

1 **Tendency Bias Correction in Coupled and Uncoupled Global Climate Models with a Focus**
2 **on Impacts over North America**

3
4
5 Y. Chang¹², S. D. Schubert¹³, R. D. Koster¹, A. M. Molod¹ and H. Wang³

6
7 ¹Global Modeling and Assimilation Office, NASA/GSFC, Greenbelt, MD

8 ²Goddard Earth Sciences Technology and Research, Morgan State University, MD

9 ³ Science Systems and Applications, Inc., Lanham, MD

10
11
12
13
14
15
16 Accepted 20 November 2018 in J. Climate

17
18
19 _____
20 *Corresponding author:* Siegfried D. Schubert, siegfried.d.schubert@nasa.gov

22 **Abstract**

23 We revisit the bias correction problem in current climate models, taking advantage of state-
24 of-the-art atmospheric reanalysis data and new data assimilation tools that simplify the
25 estimation of short-term (6-hourly) atmospheric tendency errors. The focus is on the extent to
26 which correcting biases in atmospheric tendencies improves the model’s climatology, variability,
27 and ultimately forecast skill at subseasonal and seasonal time scales. Results are presented for
28 the NASA/GMAO GEOS model in both uncoupled (atmosphere only) and coupled (atmosphere-
29 ocean) modes.

30 For the uncoupled model, the focus is on correcting a stunted North Pacific jet and a dry bias
31 over the central US during boreal summer – long-standing errors that are indeed common to
32 many current AGCMs. The results show that the tendency bias correction (TBC) eliminates the
33 jet bias and substantially increases the precipitation over the Great Plains. These changes are
34 accompanied by much improved (increased) storm track activity throughout the northern middle
35 latitudes. For the coupled model, the atmospheric TBCs produce substantial improvements in
36 the simulated mean climate and its variability, including a much reduced SST warm bias, more
37 realistic ENSO-related SST variability and teleconnections, and much improved subtropical jets
38 and related sub-monthly transient wave activity.

39 Despite these improvements, the improvement in subseasonal and seasonal forecast skill over
40 North America is only modest at best. The reasons for this, which are presumably relevant to
41 any forecast system, involve the competing influences of predictability loss with time and the
42 time it takes for climate drift to first have a significant impact on forecast skill.

43

44 **1. Introduction**

45 Substantial progress has been made over the last few decades to improve the ability of
46 climate models to reproduce the observed climate. For example, Flato et al. (2013) provide an
47 overview of the quality of the CMIP5 climate models (IPCC, 2013), including a synthesis of our
48 confidence in the ability of models to simulate various features of the 20th century climate
49 including means, various modes of variability, trends, and extremes. They conclude that overall,
50 climate models are indeed getting better in simulating climate (e.g., compared to CMIP3
51 models), providing greater confidence in the appropriateness of these models for climate change
52 studies.

53 Nevertheless, despite these overall improvements, current climate models are far from
54 perfect, and specific biases appear to be especially detrimental to forecast skill on subseasonal to
55 seasonal time scales, our focus here. For example, during boreal summer, the middle latitude
56 jets serve as wave-guides for Rossby waves entering North America and Europe (e.g., Schubert
57 et al. 2011, Wang et al. 2017). Any deficiencies in the simulation of the summer jets would
58 therefore likely affect our ability to predict Rossby wave impacts on weather and climate
59 extremes over the northern continents. During boreal winter, the hydroclimate of North America
60 is strongly affected by moisture influx from the North Pacific (e.g., Wang and Schubert 2014)
61 that is linked to North Pacific synoptic systems steered by the jet stream. Indeed, the occurrence
62 of drought along the west coast of the U.S. is especially sensitive to the strength and position of
63 the planetary waves, especially the west coast ridge (e.g., Seager et al. 2015); such waves are
64 linked to modes of internal atmospheric variability such as the Pacific North American (PNA)

65 pattern as well as to ENSO and other tropical SST anomalies (e.g., Seager et al. 2015; Seager
66 and Henderson 2016).

67 The degree of verisimilitude required in simulating these modes (as well as the mean state)
68 for improving forecast skill at subseasonal and seasonal scales is unclear. Corrections to model
69 biases can be made “after the fact”; operational forecasts can be post-processed to deal with
70 climate drift estimates determined from long histories of reforecasts (e.g., Kirtman et al. 2014),
71 and biases in variability can be corrected through such methods as quantile mapping (e.g.,
72 Cannon, 2016). Such approaches, however, can only go so far – they cannot correct, for example,
73 for the complete absence of a critical atmospheric mode or linkage during a forecast. Indeed,
74 certain forecast deficiencies can only be avoided by improving the accuracy of the model
75 simulation itself.

76 Given the difficulty of addressing certain model biases quickly through model improvement,
77 some have considered a stopgap approach: introducing empirically determined “on-line”
78 corrections to the model’s tendency equations. A number of studies have examined the impact
79 of such statistical corrections to early operational and/or simplified numerical models with a
80 focus on developing methods for improving weather forecasts (e.g., Leith 1978; Schemm and
81 Faller 1986; Saha 1992; DelSole and Hou 1999). In a recent study, Danforth et al. (2007)
82 addressed the problem of estimating and correcting model errors using two simplified but
83 realistic GCMs. They found that online state-independent corrections result in significant
84 improvements in the skill of weather forecasts, improvements that are larger than those obtained
85 with *a posteriori* corrections. They further found that state-dependent corrections resulted in
86 worse prediction skill due to sampling errors in the estimation of the full covariance matrix,
87 though they were able to obtain some improvements by localizing the covariance matrix, or

88 alternatively by introducing an SVD-based formulation of the correction operator. We note that
89 another approach, based on historical analogs, that takes into account the possible state-
90 dependence of errors has been shown to be successful (when applied after the fact) in reducing
91 biases in the planetary-scale waves in medium range forecasts (Yu et al. 2014a,b).

92 In this study, we revisit the bias correction problem, employing a state-of-the-art reanalysis
93 (MERRA-2) and modern data assimilation tools to correct the systematic model tendency errors
94 in both uncoupled (atmospheric general circulation model, AGCM) and coupled (atmospheric-
95 ocean general circulation model, AOGCM) versions of the NASA Global Modeling and
96 Assimilation Office (GMAO) GEOS model. Rather than weather forecasting, our focus here is
97 on examining the extent to which correcting the short-term model tendency biases leads to
98 improvements in some of the GEOS model's long-standing mean climate biases (e.g., in the
99 North Pacific Summer Jet (NPSJ), the boreal winter stationary waves, and the Intertropical
100 Convergence Zone (ITCZ)) – biases that are indeed found in a number of AGCMs and
101 AOGCMs. In addition, we examine whether there are any associated improvements in the
102 simulation of weather and climate variability as well as in the forecast skill attained over North
103 America at subseasonal to seasonal time scales.

104 Section 2 describes the methodology used, the GEOS model, and the experiments performed.
105 Section 3a (Section 3b) shows the impact of the bias corrections on the climatic means,
106 variances, and covariances simulated in the uncoupled (coupled) versions of the model, and
107 Section 3c examines their impact on subseasonal and seasonal forecast skill over North America.
108 Discussion and conclusions are provided in Section 4.

109

110 2. Methodology and Model Experiments

111 a. Estimating the tendency biases

112 The GEOS data assimilation system currently uses an increment analysis update (IAU)
113 procedure designed to reduce analysis-induced initial shocks in the model forecast phase of the
114 assimilation cycle (Bloom et al. 1996). The IAU procedure incorporates a constant analysis
115 increment due to each atmospheric analysis, gradually (over the course of the analysis period) as
116 a forcing term in the model tendency equations. Any non-zero long-term average of the IAU
117 increments is what we define here as the “tendency bias” of the model – a bias that presumably
118 causes the model to drift away from the reanalysis climate during the course of a long-term
119 forecast. To be clear on terminology, our use of the word “bias” refers to time mean differences
120 between the model forecasts and observations (or reanalysis) *that are functions of forecast lead-*
121 *time*. As such, the tendency bias (as defined above) and the model’s climatological bias (that
122 obtained from a free-running climate simulation) represent the two end points of the bias
123 evolution (also referred to here as the drift), with the former measuring how the model initially
124 starts to drift away from the observed climate, and the latter measuring where it ends up (after
125 the model loses all memory of the initial state). A key question we address here is to what extent
126 does correcting the initial bias correct the climatological bias of the free running model.

127 The IAU approach can be applied “after the fact” by using an existing reanalysis and a
128 sequence of short term forecasts to estimate the increments, correcting the model accordingly at
129 each time step – basically mimicking the IAU procedure used during an assimilation. Such an
130 approach, referred to as “replay” (Orbe et al. 2017; Takacs et al. 2018), can be used with an
131 existing reanalysis to force a model to remain close to that reanalysis at each time step. The

132 tendency bias correction (hereafter, TBC) method is essentially a replay but instead of applying
133 the increment from a specific forecast-analysis difference, applies a long-term averaged
134 increment (retaining the diurnal and annual cycles) at every time step. Details of the
135 methodology are provided in Appendix A. In this way, TBC takes advantage of an existing
136 assimilation or previously generated replay to estimate the long-term mean model tendency
137 biases and uses them as additional forcing terms in the model equations. It is assumed that the
138 TBCs reflect error growth that is linear and therefore should provide a reasonable estimate of the
139 biases in the model tendencies, subject to any observational/analysis biases (e.g., Xue et al.,
140 2013; Bhargava et al. 2018).

141 Since the uncoupled model used here is the same as that used to produce MERRA-2 (though
142 run at a lower resolution), the tendency bias terms for u , v , T , q , and p_s are taken directly from
143 the MERRA-2 increments for the period 1980-2015, averaged to the lower resolution (nominally
144 1°). This, while likely not optimal as compared to using a new replay to MERRA-2 at the lower
145 resolution, was done for practical reasons. Recent work suggests some dependence of the results
146 on resolution (e.g. Achuthavarier et al. 2017).

147 Our initial attempt at correcting the coupled model was to simply correct the atmospheric
148 fields (i.e., to impose the tendency bias terms derived from MERRA-2) and then couple the
149 corrected atmosphere to the ocean. This however resulted in spurious feedbacks to the
150 corrections in the tropics that apparently result from a mismatch between the atmospheric biases
151 in the coupled and uncoupled models. We instead found it necessary to carry out a replay to
152 MERRA-2 while running in coupled mode. It is important to note that, even for the coupled

153 model, we correct only atmospheric quantities¹. Thus, in our coupled simulations, the ocean is
154 only indirectly constrained by imposed corrections. There is, however, one important difference
155 between our use of TBC in our coupled and uncoupled simulations: in the coupled simulations,
156 only the fields u , v , T , and p_s are corrected with the mean increments. Specific humidity is not
157 corrected².

158

159 **b. The uncoupled and coupled GEOS-5 model**

160 The results presented here are based on two different versions of the GEOS-5 model: an
161 atmosphere-only version and a coupled atmosphere-ocean version. This allows us to address
162 different model deficiencies and their corresponding impacts on forecast skill. More generally, it
163 lets us assess the performance of the TBC approach within both coupled and uncoupled
164 environments.

165 The uncoupled GEOS model used here is the same AGCM used to generate MERRA-2,
166 though here the model is run at a coarser horizontal resolution (approximately 1°). As described
167 in Gelaro et al. (2017), this AGCM includes the finite-volume dynamical core of Putman and Lin
168 (2007), which uses a cubed sphere horizontal discretization and 72 hybrid-eta levels from the
169 surface to 0.01 hPa. Recent upgrades to the physical parameterization schemes (in going from
170 the original MERRA to MERRA-2) include increased re-evaporation of frozen precipitation and
171 cloud condensate, changes to the background gravity wave drag, and an improved relationship

¹ We did not consider trying to also correct the ocean since it is unclear that the ocean analysis are of sufficient quality to estimate the necessary biases, though this may ultimately be the best approach.

² This was done out of an initial concern about possible negative impacts on fresh water flux into the oceans, though this has since been found to not be an issue.

172 between the ocean surface roughness and ocean surface stress. The model also includes a
173 Tokioka-type trigger on deep convection as part of the Relaxed Arakawa-Schubert (RAS,
174 Moorthi and Suarez 1992) convective parameterization scheme (Bacmeister and Stephens 2011).
175 A new glaciated land representation and seasonally-varying sea ice albedo were implemented for
176 MERRA-2, leading to improved air temperatures and reduced biases in the net energy flux over
177 these surfaces (Cullather et al. 2014). The model includes the Catchment land surface model
178 developed by Koster et al. (2000). Further details about this version of the GEOS AGCM can be
179 found in Molod et al. (2015).

180 The coupled model (AOGCM) used here is part of the Subseasonal to Seasonal (S2S)
181 prediction system that is (at the time of this writing) being used by the GMAO to provide
182 forecasts to the North American Multi-Model Ensemble (NMME) project on a real time basis
183 (though here our coupled model is run at coarser resolution). The model is described in more
184 detail in Molod et al. (2018). The AGCM component of the AOGCM is a more recent version of
185 the GEOS AGCM (described above) though it is fundamentally the same as the MERRA-2
186 version. The new AGCM includes parameter changes to enhance surface drag over land and
187 oceans, to enhance form drag, and to enhance parameterized convection in the extratropics, all
188 designed to improve weather forecast skill.

189 The ocean component of the GEOS AOGCM is the Modular Ocean Model version 5
190 (MOM5) developed at the Geophysical Fluid Dynamics Laboratory described in Griffies et al.
191 (2005). The sea ice component is the CICE 4.1 model developed by the Los Alamos National
192 Laboratory (Hunke and Lipscomb 2008). The ocean and atmosphere exchange fluxes of
193 momentum, heat and fresh water through a "skin layer" interface that includes a parameterization
194 of the diurnal cycle.

195

196 **c. The experiments**

197 The AGCM and AOGCM experiments analyzed in this study are listed in Table 1. Both
198 models were forced with time varying GHGs as described in Appendix A of Schubert *et al.*
199 2014. The AGCM simulations (forced with the same observed SST and sea ice fraction used in
200 MERRA-2³) consist of: (i) a long term control simulation (CNTRL-A), and (ii) a simulation
201 (TBC-A) equivalent to CNTRL-A except for the continual correction of the model tendency
202 biases using the TBC approach, with the correction terms (in u , v , T , q and p_s) taken directly
203 from MERRA-2. The CNTRL-A model and the TBC-A model were also used to produce
204 hindcasts (with observed SST) initialized from MERRA-2. In this set of hindcasts, the hindcast
205 year's data are excluded from the estimation of the bias correction terms.

206 The AOGCM simulations consist of a long control simulation (CNTRL-C), a run replayed to
207 the MERRA-2 atmosphere fields of u , v , T , and p_s (REPLAY-C), and a third run (TBC-C) in
208 which the TBC approach is used to correct the u , v , T , and p_s tendencies, using corrections
209 estimated from REPLAY-C. In addition, seasonal hindcasts were produced using both the
210 CNTRL-C model and the TBC-C model, with initial conditions taken from REPLAY-C (again,
211 with the hindcast year's data excluded from the estimation of the bias correction terms).

212

213 **3. Results**

³ As summarized in Gelaro et al. (2017), the MERRA-2 SST are based on a combination of different high resolution daily NOAA OISST and OSTIA products, though prior to 01 Jan 1982, it is based on the CMIP mid-monthly 1° data.

214 We present here the results of applying the TBC to the GEOS model. Sections 3a and 3b
215 focus on the impacts on the climatological biases of the AGCM and AOGCM, respectively,
216 while Section 3c examines the impact on forecast skill.

217

218 **a. TBC in the uncoupled model**

219 The impact of TBC on the mean climate and climate variability in the AGCM is estimated
220 from the TBC-A and CNTRL-A simulations (see Table 1). Climatological biases are defined
221 here as long-term averaged differences from MERRA-2 and other observations as indicated
222 below.

223 Figures 1 and 2 show the impact of the TBC on the zonal mean climatological biases for DJF
224 and JJA respectively for the u-wind and specific humidity. We present, in the left panels, the
225 climatological biases (CNTRL-A – MERRA-2), in the middle panels the improvement with TBC
226 (TBC-A - MERRA-2), while in the right panels we show (TBC-A - CNTRL-A) to more clearly
227 illustrate the impact of the TBC. The zonal wind biases in CNTRL-A are characterized by a
228 poleward shift of the jets in both summer hemispheres (evident from the north/south dipole
229 structure of the differences), with some tendency for an equator-ward shift in the winter
230 hemispheres. In TBC-A, the poleward shift of the summer jets is substantially corrected,
231 especially during JJA. There is less improvement in the winter jets; in fact, the SH high latitudes
232 show, for TBC-A, an increased positive zonal wind bias during JJA (top center and right panels
233 of Fig. 2). The reason for this is unclear but likely reflects a cold bias that develops during JJA
234 throughout the troposphere over the SH polar regions in TBC-A. Section 4 provides a discussion
235 of possible reasons for why the TBC does less well in correcting the climatological biases in
236 some regions/seasons. TBC also acts to reduce substantially the zonal mean specific humidity

237 climatological biases, especially the relatively large positive biases that occur in the
238 lower/middle troposphere on either side of the equatorial moisture maximum during DJF (bottom
239 panels of Fig. 1), as well as the biases in the midlevel tropics (just south of the equatorial
240 maximum) and lower tropospheric NH middle latitudes during JJA (bottom panels of Fig. 2). We
241 note that in both seasons the TBC-A acts to correct (strengthen) the upward motion regime of the
242 tropics, so much so that the simulated Hadley cell is essentially indistinguishable from that in
243 MERRA-2 (not shown).

244 Figure 3 shows the results for the 250mb u-wind (left column), two-meter temperature over
245 land (T2m, middle column) and precipitation (right column) for JJA. Here again, we present in
246 the top panels, the climatological biases (CNTRL-A – MERRA-2), in the middle panels the
247 improvement with TBC (TBC-A - MERRA-2), while in the bottom panels we show (TBC-A -
248 CNTRL-A) to more clearly illustrate the impact of the TBC. The impact of TBC-A is to
249 eliminate almost completely the prevailing zonal wind climatological biases throughout the NH,
250 especially the weak jet in the North Pacific. In the SH, where the biases are much weaker to start
251 with, TBC-A is less effective, and in fact (as we saw in Fig. 1) generates a positive zonal wind
252 bias at high latitudes. In the NH, the impact of TBC-A on JJA T2m is remarkable, as it
253 eliminates most of the large positive biases, especially those over Asia and North America. The
254 climatological precipitation biases (top right panel of Fig. 3) also show substantial improvement
255 in many regions, with a reduction of large biases over Tibet, the maritime continent, the ITCZ,
256 the NH storm tracks, and North America (middle right panel of Fig.3): impacts which are
257 perhaps more clearly seen from the TBC-A – CNTRL-A fields in the bottom right panel of Fig.
258 3. Particularly noteworthy is the substantial reduction in the dry bias over the US Great Plains, a
259 long-standing problem in the GEOS model and many other climate models (e.g, Lin et al. 2017).

260 The TBC-A impact, however, is not positive everywhere, with the increased wet bias over India
261 being perhaps the most glaring deficiency.

262 We next turn our attention to the transients during JJA (Figure 4). These are based on 6
263 hourly data (with the monthly means removed) and include the time mean vertically-integrated
264 zonal momentum transport ($\overline{u'v'}$, left panels), the 250mb meridional wind variability ($\overline{v'^2}$,
265 middle panels – a measure of storm track activity [e.g., Chang and Fu 2002]), and the 850mb
266 moisture transport ($\overline{v'q'}$, right panels). The climatological biases in all three quantities are
267 apparent, and there are substantial corrections in the NH with TBC-A. In particular, substantial
268 improvements are seen in the NH momentum transport, especially in the North Pacific and North
269 Atlantic jet exit regions, where the high frequency eddies are expected to maintain the mean jet
270 through barotropic decay (e.g., Chang et al. 2002). Also, the negative biases in $\overline{v'^2}$ (indicating
271 weak storm tracks) seen in CNTRL-A, especially in the eastern North Pacific and the North
272 Atlantic, are reduced in TBC-A by more than a factor of two in many places, an improvement
273 that occurs in conjunction with the improved (strengthened) jet in these regions. Similar
274 improvements are seen for moisture transport, with substantial increases in northward transport
275 in the NH storm tracks in TBC-A. Also of note for TBC-A is the increased northward moisture
276 transport over the central US, an improvement that very likely contributes to the aforementioned
277 increased precipitation in this region. The TBC appears to be less effective in improving the JJA
278 transients in the SH, especially over the high latitude oceans.

279

280 **b. TBC in the coupled Model**

281 We now examine the impact of applying the atmospheric TBCs obtained from REPLAY-C
282 to the fully coupled GEOS-5 AOGCM. In assessing the impact of TBC, we compare the TBC-C

283 results to those from both the CNTRL-C and the REPLAY-C runs. As described in Section 2,
284 the replay approach allows us to force any model to remain close to the reanalysis during the
285 course of an integration, providing as a byproduct the information needed to compute the TBC
286 terms. If the model used in the replay is identical to that used to produce the original reanalysis,
287 then one simply reproduces that reanalysis exactly. If, on the other hand, the modeling system
288 differs from that of the reanalysis (as it does here, for three reasons: we use an updated AGCM
289 [see above], we couple this AGCM to an ocean model, and we run at a lower resolution),
290 identical results are not guaranteed, especially for quantities (e.g., precipitation) that are not
291 directly constrained by the analysis increments. Given these considerations, the “replayed”
292 results (REPLAY-C) can be considered an upper bound to what can be achieved from the TBC.
293 Further details of the replay approach and some caveats concerning the stability of the procedure
294 can be found in Takacs et al (2018).

295 Figure 5 (left panels) shows the biases for the annual mean SST. The top left panel shows
296 that the replay approach (REPLAY-C) is able, for the most part, to reproduce the annual mean
297 observed (Reynolds) SST. In contrast, the free-running CNTRL-C (middle left panel) shows
298 large positive SST biases over much of the tropics and SH. These biases are essentially
299 eliminated when TBC is applied (bottom left). In fact the performance of the TBC-C simulation
300 is quite similar to that of REPLAY-C over much of the world’s oceans. TBC-C also reduces the
301 cold biases in the North Pacific, though not to the extent seen in REPLAY-C. While TBC-C
302 provides little improvement in the tropical SST annual cycle (not shown), this cycle is already
303 fairly realistic in CNTRL-C. In fact, TBC-C seems to have introduced a slightly exaggerated
304 annual cycle in the central Pacific.

305 The impact of TBC-C on tropical SST variability is shown in the right three panels of Figure
306 5. CNTRL-C clearly has excessive variability (tied to ENSO) compared with the observations.
307 In contrast, the variability in the TBC-C run has more reasonable amplitude, though TBC does
308 miss very strong events of the type that occurred in nature during this time period (e.g., 1982/83,
309 1997/98, 2015/16)⁴. As a result, the overall SST variability in TBC-C is somewhat weaker than
310 the observed variability.

311 Turning next to the results for the zonal mean atmosphere, TBC-C produces substantial
312 reductions in the biases of the zonal mean zonal wind almost everywhere (and especially in the
313 subtropics) for both seasons (top panels of Figs. 6 and 7). The improvement in the zonal mean
314 specific humidity (bottom panels of Fig. 6 and 7) is also substantial, highlighted by the
315 elimination of the wet biases in CNTRL-C in the tropics and SH during both seasons (it is
316 noteworthy that this occurs despite not correcting the moisture). We note that the TBC-C
317 produces little improvement in the zonal mean vertical motion during DJF (not shown) in
318 contrast to the improvement seen in the AGCM simulations. However, there is a rather
319 substantial improvement during JJA including a reduction in the anomalous upward motion in
320 the upper troposphere just north of the equator.

321 Figure 8 shows the biases in the DJF (left panels) and JJA (right panels) precipitation for
322 REPLAY-C (top panels), CNTRL-C (middle panels), and TBC-C (bottom panels). We see that
323 much of the excessive precipitation that occurs just north of the equator in the Pacific during
324 both seasons in CNTRL-C is reduced in the REPLAY-C run, as is the excessive precipitation in
325 the tropical Atlantic and the Indian Ocean. The large dry bias over India and wet bias over

⁴ We note that there is no reason for the simulations to have ENSO events synchronized with those in nature, though the models are run with observed CO₂ and other greenhouse gases, explaining the positive trend seen in the SST in both the observed and simulated SSTs.

326 Southeast Asia during JJA in CNTRL-C are also reduced in REPLAY-C. REPLAY-C does
327 introduce a substantial dry bias over South America during DJF that is not evident in CNTRL-C.
328 REPLAY-C also does little to reduce the dry bias over the US Great Plains; in fact it appears to
329 exacerbate it compared to the control. Since winds and temperature in the replay are essentially
330 the same as those in MERRA-2, the lack of improvement in the precipitation over the US Great
331 Plains and the other regions mentioned above almost certainly reflects the fact that we do not
332 replay the moisture in the AOGCM.

333 The TBC-C run produces some of the same improvements indicated above for the REPLAY-
334 C run. The TBC-C is, however, less effective in reducing the excessive Pacific precipitation that
335 occurs north of the equator, especially during DJF; in fact, TBC-C appears to be slightly worse
336 than CNTRL-C in the eastern tropical Pacific, with a dry bias just south of the equator and a
337 somewhat larger wet bias south of that. During JJA, TBC-C successfully reduces the dry bias
338 over India, reduces the wet bias over Southeast Asia, and is somewhat more successful
339 (compared with DJF) in reducing the excessive precipitation over the tropical Pacific.

340 We note that while TBC-C does produce overall more realistic atmospheric (e.g., OLR)
341 variability in the tropics, primarily by reducing the excessive variance found in the CNTRL-C
342 run (not shown), it does little to improve the MJO, though the CNTRL-C model already
343 produces a fairly realistic but weaker-than-observed MJO (D. Achuthavarier, personal
344 communication).

345 We next focus on DJF, with an eye towards assessing how TBC-C affects ENSO-related
346 teleconnections over North America during that season. Since ENSO has large impacts on the
347 North Pacific/North American jet and stationary waves, improvements in the climatologies of
348 those aspects of the flow should have positive impacts on ENSO-related teleconnections. Figure

349 9 (left panels) shows that TBC-C corrects the excessive subtropical westerly winds that extend
350 across the North Pacific, the southern United States, and the North Atlantic. It also eliminates
351 the easterly bias in the eastern tropical Pacific. It does little to correct the relatively small biases
352 seen for CNTRL-C in the SH. The TBC-C run also substantially improves the boreal winter
353 stationary waves (right 3 panels of Fig. 9), particularly the position, structure and amplitude of
354 both the ridge over the west coast of North America and the upstream trough.

355 Turning next to the DJF transients (Fig. 10), we see that CNTRL-C has anomalously large
356 transient wave activity (as reflected in the 250mb kinetic energy, left panel) centered at about
357 30°N and generally over the continents. This bias, which is presumably linked to the excessive
358 subtropical westerlies noted earlier, is corrected in the TBC-C run. In fact, TBC features
359 transients that, compared to MERRA-2, are slightly too weak in the NH and, while somewhat
360 improved, remain too weak in the SH. TBC-C shows large improvements in the NH 200mb
361 zonal momentum flux (middle panels) and also shows improvements in the 850mb transient
362 moisture transport (right panels), particularly just south of the storm track regions.

363 On interannual time scales, TBC-C primarily acts to reduce some of the excessive DJF
364 stationary wave variance that occurs in CNTRL-C over the northeast Pacific, northern Eurasia
365 and eastern North America (left 3 panels of Fig. 11). While these impacts are positive overall,
366 the reduction over the eastern North Pacific results in a variability that is now somewhat too
367 weak. The reductions are likely due to TBC-C-induced changes in the (now reduced) variability
368 of the tropical Pacific SST linked to ENSO, which is known to contribute to the height
369 variability over the North Pacific/North American region (e.g., Diaz et al. 2001). The
370 interannual link between the tropical Pacific SST and the 250mb eddy height field for DJF is
371 quantified in Figure 11 (right panels) in terms of the correlation between eddy height and the

372 Nino3.4 index. TBC-C shows a weakening of certain biases seen in CNTRL-C, particularly the
373 unrealistically strong negative correlations over much of the United States and southern Canada
374 and the strong positive correlations to the north. The overall spatial pattern of the correlations
375 over the North Pacific/North American region is also improved.

376

377 **3c. Forecast Skill**

378 In this section we assess the degree to which TBC increases forecast skill over North
379 America in both the uncoupled (Section 3ci) and coupled model (section 3cii). In the uncoupled
380 case, we focus on boreal summer and subseasonal time scales, for which coupling to the ocean is
381 likely of secondary importance. In the coupled case, we focus on boreal winter and seasonal
382 time scales, for which ENSO is known to have an important impact on forecast skill.

383 *i. Boreal Summer and the uncoupled model*

384 Our focus here is on the extent to which the improvements in the subtropical/middle latitude
385 jets and transients in the TBC-A model described in Section 3a lead to improvements in
386 subseasonal boreal summer forecast skill over North America. The skill assessment is based on
387 a series of hindcasts initialized in late spring and running through August produced with both the
388 CNTRL-A and TBC-A models (see section 2c). Note that in the following we use the
389 terminology hindcasts and forecasts interchangeably, keeping in mind that these simulations are
390 not true forecasts; in these atmosphere-only runs, observed SSTs are prescribed throughout the
391 forecast period.

392 The connection between forecast skill and the quality of a model's climate (including
393 variability) is not straightforward, though it seems plausible that a model with a better long-term

394 climate should have better forecast skill. Even if that is the case, correcting climate drift (which
 395 is a function of forecast lead time, see Section 2a) can presumably only lead to improved forecast
 396 skill if a substantial amount of the bias (and its correction) occurs before all predictability is lost.
 397 Therefore, these two time scales (associated with drift development and predictability) serve to
 398 define a window of forecast leads during which TBC can be expected to have an impact on skill.
 399 For example, if it turns out that it takes 3 months for the drift in the CNTRL to fully develop into
 400 the long-term climate bias, and if the underlying predictability limit is 20 days, it is unlikely that
 401 any small correction (made by TBC) to the still small bias in the CNTRL during the first 20 days
 402 would have much impact on forecast skill. In order to help address this issue we decompose the
 403 total mean square error (MSE) into the following terms:

404

$$\overline{\langle (F - O)^2 \rangle} = \overline{[\langle F \rangle - \langle O \rangle]^2} + \overline{\langle (F - \langle F \rangle)^2 \rangle} + (\overline{\langle F \rangle} - \bar{O})^2, \quad (1)$$

406

407 where the angle brackets denote an ensemble mean and the over-bar a time mean; also F denotes
 408 a forecast and O denotes the observations (MERRA-2). The first term on the right hand side
 409 (RHS) is the MSE after first removing the respective time means. We will refer to this term as
 410 the unbiased MSE. The second term on the RHS is the MSE of a perfect model (the ensemble
 411 mean predicting one ensemble member), and the third term is the MSE associated with the
 412 climate drift. This latter term quantifies the evolution of the bias or drift as discussed earlier,
 413 saturating at long leads (when the forecast has lost all memory of the initial conditions) to the
 414 square of the climatological bias.

415 The top left panel in Fig. 12 shows the decomposition for the 250mb u-wind (in terms of
416 RMSE, averaged over the NH)⁵, and the middle left panel shows the decomposition for the
417 250mb v-wind (averaged over the middle latitude North Pacific). These two quantities should
418 give us a sense for how the drift in the wave-guide evolves (u250mb) and the extent to which the
419 Rossby waves themselves are predicted more accurately (v250mb). Both the u-wind and the v-
420 wind total errors (blue curves) saturate by about 15 days (slightly longer for the u-wind)
421 regardless of whether the model is corrected or not. This reflects the underlying predictability
422 limits of the model (red curves), which is about 20 days. The unbiased RMSE (black curves)
423 indicate no improvement in the v-wind TBC-A skill compared to CNTRL-A by this metric. The
424 bottom left panel of Fig. 12 shows that there is, however, apparently some very modest
425 improvement in the correlation beginning somewhat before day 10, though this occurs only after
426 the skill for both CNTRL-A and TBC-A is rather small (about 0.3). To assess whether these
427 averaged results represent significant improvements we show in the right panels of Fig. 12 an
428 example of the spatial distribution of the correlations at a lead of 12 days. The differences show
429 generally positive values with statistically significant improvements along the storm track – the
430 region we would expect to see improvements in light of the improved North Pacific jet. We note
431 that in comparison, the perfect model correlations are substantially larger than the actual
432 correlations, (above 0.4 at 10 days), suggesting that further improvements in skill may be
433 possible.

434 The fact that the improvement in the v-wind is modest and doesn't occur until after the first
435 week in the forecasts likely reflects the fact that the bias in the u-wind (the wave guide) develops

⁵ The values are obtained by first computing the MSE at each gridpoint. These values are then averaged over the indicated regions, after which the square root is taken to obtain the RMSE. Correlations are computed similarly with the covariances computed at each grid point and then averaged over the indicated regions.

436 slowly over the course of about 2 months (green curves in top left panel of Figure 12). As a
437 result, any impacts on T2m and precipitation forecast skill over North America from the
438 improvements in the wind forecasts are likely confined to week two (after that the v-wind skill is
439 likely too low (< 0.1) to have an impact. Ultimately the longest lead times at which we can
440 expect some improvement are constrained by the v-wind limit of predictability, which is about
441 20 days. Having said that, we find essentially no improvement in North American precipitation
442 forecasts with TBC at those leads (not shown). On the other hand, we do find some
443 improvement in T2m forecasts (Fig. 13), especially when we condition the forecasts on the
444 amplitude of the leading Rossby wave impacting North American climate in summer (lower left
445 panel of Fig 13; see also Schubert et al, 2011). The results shown for day 10 (top right panel of
446 Fig. 13) indicate that some of the largest improvements occur over Canada, consistent with
447 where we expect the leading Rossby wave to have the greatest impact on T2m (lower right panel
448 of Fig 13). This increased skill in predicting T2m apparently reflects the fact that the leading
449 RCEOF is forecast with greater skill in the TBC-A hindcasts after the first week (not shown).

450

451 *ii. Boreal Winter and the Coupled Model*

452 Our focus here is on whether the TBC approach applied to the coupled model leads to
453 improved boreal winter seasonal forecasts, especially over North America, where we expect that
454 any improvements in SST variability, stationary waves, and ENSO-related teleconnections might
455 translate into improved forecast skill. The forecasts were initialized on 1 November of 1985-
456 2015 and consist of 10 ensemble members for both the CNTRL-C and TBC-C models (see
457 Section 2c).

458 Figure 14 (top two panels) again provides an integrated overview of the coupled hindcast
459 results decomposed into the various terms of (1), focusing in this case on the eddy 250mb height
460 field. Averaged over the NH (top panel), the total error appears to saturate after about two
461 months (in January), with CNTRL-C showing larger total error than TBC-C. The larger total
462 variance of the CNTRL-C appears to reflect an intrinsic property of the models (evident in the
463 perfect model results – the red curves), but it is also in part due to the development of a larger
464 bias in the control (green curves) both early in the forecast (November/early December) and
465 again starting in January. The perfect model RMSE approaches the unbiased RMSE (black
466 curves) by mid-December, indicating that most of the predictability (based on RMSE) is lost by
467 that time. In early February there is some hint that the TBC-C predictions have somewhat
468 smaller unbiased RMSE than the control (black curves). For comparison, the results for the SH
469 indicate little difference between the TBC-C and CNTRL-C hindcasts in either the drift or
470 RMSE, consistent with the less substantial TBC-derived improvement to the SH climate.

471 The bottom panel of Figure 14 shows the correlations with MERRA-2 for the PNA region
472 (150°E-300°E, 20°N-80°N). The perfect model and TBC-C correlations with MERRA-2 both
473 drop to 0.3 by the beginning of December, the time at which the NH RMSE approaches
474 saturation. The control correlations with MERRA-2 drop even faster, reaching 0.2 by this time.
475 There is however, some indication of a return of skill during January and February in the perfect
476 model results, presumably linked to the stronger impact of ENSO over some parts of North
477 America during these months (e.g., Jong et al. 2016). The return of skill is also evident in the
478 TBC-C hindcasts, though less so in the control hindcasts. The apparent increase in skill during
479 February is consistent with Chen et al. (2017), who found that, for ENSO-related T2m and

480 precipitation predictions over North America, the skill for all of the NMME models tended to be
481 higher in February than in other winter months.

482 The evolution of the climate drift in the 250mb eddy height fields (and the correlations)
483 shown in Figure 14 suggests that any improvement in wintertime seasonal forecast skill from
484 TBC-C over North America is likely to occur early on (during the first month of the forecast)
485 and late in the forecast at lead times beyond roughly 2 months.

486 The left set of 9 plots in Figure 15 show the hindcast skill of the 250mb eddy height over the
487 Pacific/North American region averaged over the early (16Nov-15Dec), middle (16Dec-15Jan),
488 and later (21Jan-01Mar) segments of the predictions. The correlations (with MERRA-2) are
489 shown for the CNTRL-C (middle row) and TBC-C (top row) hindcasts; differences are shown in
490 the bottom row. The correlations in both sets of hindcasts are overall, as expected, high over the
491 tropics/subtropics, with some relatively high correlations (>0.6) also occurring over the North
492 Pacific, western North America and the southeast US. Over North America, the difference maps
493 show some improvement in skill for the TBC-C height hindcasts for the early segment and again
494 some improvement for the late segment (though marginally significant), with no improvement
495 for the middle segment – results that are consistent with the line plots of the correlations in Fig.
496 14. These apparent improvements in the skill of the eddy height predictions occur in the absence
497 of any significant improvements in the tropical Pacific SST forecasts (not shown).

498 The middle (right) set of 9 panels of Figure 15 show the correlations for T2m (precipitation)
499 over North America. As with the eddy heights, the largest improvements for T2m hindcasts
500 occur early on and again late in the forecasts, with no skill, or even reduced skill, compared to
501 CNTRL-C for the interval in between. For precipitation, TBC shows overall little improvement
502 in skill, with some scattered improvements along the west coast early in the forecast. During the

503 middle period, TBC-C actually shows substantial areas of degraded skill relative to CNTRL-C
504 especially over the southeastern US.

505

506 **4. Discussion and Conclusions**

507 This study examined the overall impact of correcting biases in short-term atmospheric
508 tendencies in a general circulation model. Results are presented for two different versions of the
509 NASA/GMAO GEOS model (an AGCM forced with observed SST, and an updated AGCM
510 coupled to an ocean model). Our experiments show that state-independent TBC to the
511 atmosphere can produce considerable improvements to the simulated mean climate as well as to
512 its variability on subseasonal and, to some extent, seasonal and longer time scales. The
513 improvements are, however, not uniform and depend to some degree on the quantity, region, and
514 season, as well as the model itself.

515 In discussing the TBC impacts on the model's climate, it is useful to consider them as being
516 divided into those that are direct and those that are indirect, with the latter including any
517 quantities (such as precipitation and, for the AOGCM, atmospheric moisture) that are not
518 explicitly forced by the TBC, as well as the transients, since the TBC is a constant forcing term.
519 It should be emphasized, however, that even for those quantities directly forced by the TBC (e.g.,
520 u , v , T), it is not a forgone conclusion that the tendency errors in these terms will be fully
521 corrected by constant forcing terms. There are several possible reasons for this including the
522 possibility that the true errors cannot be represented by a simple constant forcing term and are in
523 fact state dependent (e.g., Leith 1978, Danforth et al. 2007), as well as the possibility that, even if
524 the errors can be represented in that way, the TBCs may be poor estimates of the true corrections

525 as a result of statistical sampling errors and/or as a result of deficiencies/biases in the reanalysis.
526 Furthermore, it is not obvious that a model will respond to the increments in a physically realistic
527 way. It is quite possible that, for example, correcting the moisture and temperature profiles
528 would lead to spurious feedbacks from the model's convective scheme, which may have been
529 tuned to produce realistic precipitation with somewhat different profiles. In the following, we
530 provide some examples from our results that serve to illustrate these issues.

531 The improvements in the middle latitude transients in both the AGCM and AOGCM are a
532 clear example of a positive indirect impact – an impact that is very likely strongly tied to the
533 improvements in the jets. The nature of the improvements in the jets (or lack of improvement in
534 some cases) appears to vary with the seasons, the hemisphere, and the model in question. TBC-A
535 corrects the poleward shift of both summer jets, consistent with increased drag on the jets (e.g.,
536 Robinson 1997). Since the summer jets are largely eddy driven (e.g., Lachmy and Harnik,
537 2016), it is likely that the improvement in the jets also drives (and interacts with) the improved
538 transient eddy momentum transport. Additional work (not shown) indicates that jet biases
539 throughout the Northern Hemisphere are particularly sensitive to temperature errors over and
540 near Tibet, suggesting that corrections in this area may be especially important in correcting the
541 NH summer jets (an example of a positive indirect impact). The TBC-A does less well in
542 correcting the high latitude zonal winds in the SH upper troposphere/lower stratosphere during
543 winter, suggesting that uncorrected errors in stratospheric dynamics and reanalysis quality (poor
544 estimates of the increments) may be issues.

545 The primary zonal wind errors in the AOGCM appear to be fundamentally different in
546 character compared with the AGCM errors, consisting of excessive subtropical westerlies in both
547 hemispheres (though more so in the NH) and during both seasons. These likely reflect

548 anomalous forcing/heating by the excessively strong and split ITCZ in the coupled model. The
549 fact that the TBC-C corrects these zonal wind errors (and associated transients), yet makes only
550 modest corrections to the tropical precipitation (especially during DJF), indicates that the
551 corrections to the zonal wind errors are forced more directly by the increments. In fact, it
552 appears that it is the tropical mid-tropospheric temperature increments that appear to play a key
553 role during DJF, presumably in part by reducing the strong tropical warm bias in that run. At
554 longer time scales, the impacts on the variability of the SST (and the associated changes in
555 tropospheric height variability) in the TBC-C run is likely tied to improvements in the equatorial
556 surface stress (not shown), though exactly how that acts to reduce the ENSO variability is
557 unclear. We note that the dramatic reduction of the SST bias in TBC-C appears to be the result
558 of a combination of direct impacts from the near surface temperature increments (especially over
559 the Gulf Stream, the SH high latitudes, and equatorial and coastal upwelling regions) and indirect
560 impacts due to the reductions in surface stress biases.⁶

561 Perhaps the strongest test of the TBC for improving the climate characteristics of the model
562 is the extent to which the components of the hydrological cycle are improved. We have seen
563 clear improvements in the precipitation in the AGCM results, both in the tropics and in the US
564 Great Plains. Also, improved (increased) cloudiness in TBC-A (not shown) appears to
565 contribute to the dramatic reduction in the warm bias over the NH summer continents. Here we
566 have a clear case where the TBC impacts are indirect; the model's parameterizations of moisture
567 processes working with the states directly affected by TBC appear to produce more realistic
568 output – a result likely helped by the fact that the AGCM is the same as that used to generate

⁶ The bias in cloud fraction has actually increased in TBC-C (less cloudiness), indicating this did not contribute to the reduction in the SST warm bias.

569 MERRA-2 (though run at lower resolution). In contrast, TBC-C produced considerably less
570 improvement to the precipitation, including little improvement to the ITCZ (especially during
571 DJF), but also no improvement to the summer dry bias over the US Great Plains. Here it is
572 instructive to compare the TBC-C and REPLAY-C runs. To a large extent the lack of
573 improvement (or even degradation as seen over South America in DJF) in the TBC-C run is
574 already reflected in REPLAY-C run. As such, this does not appear to reflect a limitation of the
575 TBC approach, but instead an inconsistent or lack of forcing by the increments (recall that we
576 don't correct the moisture in the AOGCM).

577 A key goal of this study was to determine whether the improved climate characteristics of the
578 model induced by TBC translate into improved forecast skill (perhaps the ultimate indirect
579 impact). We found, however, that TBC-related skill improvements were rather modest at best at
580 both subseasonal and seasonal time scales. For the uncoupled case, where our focus was on
581 boreal summer and subseasonal forecasts, the improvements in the NPSJ and the transient eddy
582 activity led to only modest improvements in the T2m forecasts over North America (and only
583 when conditioned on the leading Rossby wave impacting North America), and to no
584 improvement in the precipitation forecasts. In the coupled case, our focus was on improving
585 boreal winter forecast skill over North America at seasonal time scales. Here too, despite
586 various improvements to the stationary waves and related transients, and despite what appear to
587 be more realistic ENSO variability and associated teleconnections, the impact of TBC on skill
588 was not uniform with forecast lead and was again overall quite modest.

589 We interpret these hindcast results in terms of predictability limits and the time it takes the
590 relevant aspects of climate drift to become large enough to begin having an impact on skill (and
591 thus the time it would take for TBC-based reductions of the drift to affect the skill). In the

592 uncoupled case, focusing on boreal summer and North America, the climate drift in the North
593 Pacific waveguide (believed to be a key controlling factor for Rossby waves entering North
594 America) appears to develop too slowly in CNTRL-A (reaching only about ½ the long term
595 value at 10 days lead) to allow its correction in TBC-A to produce more than a modest impact
596 (via more skillful Rossby wave predictions) on week-two T2m forecasts (when skill is already
597 rather low). In the coupled case, focusing on boreal winter over North America, our assessment
598 of the drift in the stationary waves suggests two adjustment time scales: an early drift that
599 develops during the first month (presumably dynamically driven) and a more slowly developing
600 drift that occurs during months 3 and 4 (presumably linked to deficiencies in coupled processes).
601 In contrast, the corrected model experienced an early drift that took longer to develop than in the
602 control, and never experienced the slow drift of the control model during months 3 and 4. There
603 thus appear to be two windows (one early and one late) during which TBC could induce
604 improved forecasts. This indeed appears to be borne out in the forecasts of both eddy heights
605 over the Pacific/North American region and T2m over North America.

606 Additional improvements in forecast skill might be possible with a state-dependent
607 correction if the associated statistical sampling issues can be overcome (e.g., Leith 1978;
608 Danforth et al. 2007). In fact, it is possible that the modest impacts on skill (or even reductions
609 in skill) found here reflect the presence of state-dependent errors that may or may not be in phase
610 with the state-independent errors. Our TBC approach nevertheless provides a reasonable
611 baseline of what can currently be achieved with state-independent corrections to a global climate
612 model employing a state-of-the-art atmospheric reanalysis. The approach is relatively easy-to-
613 implement and, since it is based on very short-term forecasts when the error growth is still linear,

614 appears to produce corrections that (to a large extent) reflect physically realistic adjustments to
615 the model equations.

616 It is however likely that substantial further improvements will require model system
617 improvements not directly addressed by TBC, improvements involving, for example,
618 land/atmosphere interaction, cloud/radiative processes, and initialization procedures for (and
619 quality of) atmospheric, land and ocean states. While potential improvements in forecast skill
620 may not be the main impetus for carrying out the TBC, we believe that TBC-induced
621 improvements in transients, stationary waves, and other climate characteristics can be a key
622 motivating factor for employing the approach. Such improvements can make the model better
623 suited for addressing a host of climate problems, such as those that require addressing regional
624 impacts of global climate variability and change.

625

626

627 **Acknowledgements**

628 This work was supported by the NASA MAP (NNG17HP01C and WBS 802678.02.17.01.33),
629 and NOAA MAPP (NA14OAR4310221) programs.

630

631

632

Appendix A: Methodology

633 As described in Takacs et al (2018), the replay approach takes advantage of the incremental
634 analysis update (IAU) procedure employed in the GEOS data assimilation system to force a
635 model to track a pre-existing analysis. The basic approach is shown schematically in Figure A1.
636 The blue arrows indicate that the replay is essentially a continuous model simulation that is
637 driven by a sequence of IAU forcing terms (updated every 6 hours) computed as the difference
638 between a short forecast and the corresponding analysis. The general form of the equations
639 governing a replay can be written (for a quantity q) as:

$$640 \quad \frac{\partial q}{\partial t} = f(q) + \Delta q \quad (A1),$$

641 where $\Delta q = (analysis - forecast)/6hrs$, and $f(q)$ is the tendency associated with all the
642 dynamics and physics terms of the model – in other words, it corresponds to the uncorrected
643 model. For the coupled model replay performed as part of this study, the increments are
644 computed for the winds, temperature and surface pressure.

645 The governing equations for the TBC approach have the same form as (1), except that the
646 forcing term associated with the increments is no longer an instantaneous value (specific to a
647 particular 6 hour period), but is instead a long term mean. In particular,

$$648 \quad \frac{\partial q}{\partial t} = f(q) + \overline{\Delta q} \quad (A2),$$

649 where the $\overline{\Delta q}$ are 6-hourly values that are averaged over the years 1980-2015 separately for each
650 6-hr time period of each day-of-year⁷, and as such retain the diurnal and annual cycles. The

⁷ In the case of the coupled model we further apply a 7-day running mean to the increments, though this is done in a way that retains the mean diurnal cycle.

651 above indicates that the model with the TBC (A2) can be considered as an approximation of
652 (A1), in which the correction term is simplified to retain only the first moment statistics (the
653 mean) of the increments: the assumption being that such simple corrections nevertheless
654 represent physically realistic systematic adjustments to the model's physics and/or dynamics
655 tendency terms.

656 As noted in the text, in the case of the AGCM, instead of replaying to MERRA-2 to obtain the
657 Δq terms, we take advantage of the fact that the AGCM used here is the same as that used to
658 generate MERRA-2 (though run at lower resolution) and so we take the increments directly from
659 the MERRA-2 archive (appropriately averaged to the reduced resolution of the AGCM). This
660 was not the case for the AOGCM. We could not simply couple the corrected AGCM to the
661 ocean, but found it necessary to replay to the MERRA-2 atmosphere running in coupled mode to
662 obtain the increments appropriate for correcting the biases that develop in the coupled model.

663 Finally, in assessing the quality of the climates of the TBC simulations, the above makes it clear
664 that the most fair comparison to make is with the climate of the corresponding replay run, as we
665 do for the coupled model. In the case of the AGCM (which is a lower resolution version of the
666 same model used to produce MERRA-2) such a comparison is, however, essentially equivalent
667 to comparing with MERRA-2, since (A1) would to a large extent reproduce the reanalysis,
668 though of course at lower resolution.

669

670 **References:**

671

672 Achuthavarier D., H. Wang, S. Schubert and M. Sienkiewicz, 2017: Impact of DYNAMO
673 observations on the NASA GEOS-5 reanalysis and the representation of the MJO
674 initiation over the tropical Indian Ocean. *J. Geophys. Res.-Atmos.* 122, 179–201,
675 doi:10.1002/2016JD025363.

676 Bacmeister, J. T., and G. L. Stephens, 2011: Spatial statistics of likely convective clouds in
677 CloudSat data, *J. Geophys. Res.*, 116, D04104, doi:10.1029/2010JD014444.

678 Bhargava, K., E. Kalnay, J.A. Carton and F. Yang, 2018: Estimation of systematic errors in the
679 GFS using analysis increments. *J. Geophys. Res.: Atmospheres*, 123, 1626 – 1637.
680 <https://doi.org/10.1002/2017JD027423>.

681 Bloom, S.C., L.L. Takacs, A.M. da Silva, and D. Ledvina, 1996: Data Assimilation Using
682 Incremental Analysis Updates. *Mon. Wea. Rev.*, 124, 1256–1271,
683 [https://doi.org/10.1175/1520-0493\(1996\)124<1256:DAUIAU>2.0.CO;2](https://doi.org/10.1175/1520-0493(1996)124<1256:DAUIAU>2.0.CO;2).

684 Cannon, A.J., 2016: Multivariate Bias Correction of Climate Model Output: Matching Marginal
685 Distributions and Intervariable Dependence Structure. *J. Climate*, 29, 7045–7064,
686 <https://doi.org/10.1175/JCLI-D-15-0679.1>

687 Chang, E. K. M. and Y. Fu, 2002: Interdecadal variations in Northern Hemisphere winter storm
688 track intensity. *J. Climate*, 15, 642–658.

689 Chang, E.K., S. Lee, and K.L. Swanson, 2002: Storm Track Dynamics. *J. Climate*, 15, 2163–
690 2183, [https://doi.org/10.1175/1520-0442\(2002\)015<02163:STD>2.0.CO;2](https://doi.org/10.1175/1520-0442(2002)015<02163:STD>2.0.CO;2)

691 Chang, Y., S. D. Schubert, S. J. Lin, S. Nebuda, B.-W. Shen, 2001. The Climate of the FVCCM-
692 3 Model. NASA *Technical Report Series on Global and Data Assimilation 104606*, Vol.
693 20. M. Suarez, editor, Document (8273 kB).

694 Chen, L., H. van den Dool, E. Becker, and Q. Zhang, 2017: ENSO Precipitation and
695 Temperature Forecasts in the North American Multimodel Ensemble: Composite
696 Analysis and Validation. *J. Climate*, 30, 1103–1125, [https://doi.org/10.1175/JCLI-D-15-](https://doi.org/10.1175/JCLI-D-15-0903.1)
697 0903.1

698 Cullather, R. I., S. M. J. Nowicki, B. Zhao, and M. J. Suárez, 2014: Evaluation of the surface
699 representation of the Greenland Ice Sheet in a general circulation model. *J. Climate*, 27,
700 4835–4856, doi:<https://doi.org/10.1175/JCLI-D-13-00635.1>.

701 Danforth, C.M., E. Kalnay, and T. Miyoshi, 2007: Estimating and Correcting Global Weather
702 Model Error. *Mon. Wea. Rev.*, 135, 281–299, <https://doi.org/10.1175/MWR3289.1>.

703 DelSole, T., and A. Y. Hou, 1999: Empirical correction of a dynamical model. Part I:
704 Fundamental issues. *Mon. Wea. Rev.*, 127, 2533–2545.

705 Diaz, H. F., M. P. Hoerling, and J. K. Eischeid, 2001: ENSO variability, teleconnections and
706 climate change. *Int. J. Climatol.*, 21, 1845–1862, doi:<https://doi.org/10.1002/joc.631>

707 Flato, G., J. Marotzke, B. Abiodun, P. Braconnot, S.C. Chou, W. Collins, P. Cox, F. Driouech, S.
708 Emori, V. Eyring, C. Forest, P. Gleckler, E. Guilyardi, C. Jakob, V. Kattsov, C. Reason
709 and M. Rummukainen, 2013: Evaluation of Climate Models. In: *Climate Change 2013:*
710 *The Physical Science Basis. Contribution of Working Group I to the Fifth Assessment*
711 *Report of the Intergovernmental Panel on Climate Change*[Stocker, T.F., D. Qin, G.-K.
712 Plattner, M. Tignor, S.K. Allen, J. Boschung, A. Nauels, Y. Xia, V. Bex and P.M.

713 Midgley (eds.)]. Cambridge University Press, Cambridge, United Kingdom and New
714 York, NY, USA.

715 Gelaro, R., W. McCarty, M.J. Suárez, R. Todling, A. Molod, L. Takacs, C.A. Randles, A.
716 Darmenov, M.G. Bosilovich, R. Reichle, K. Wargan, L. Coy, R. Cullather, C. Draper, S.
717 Akella, V. Buchard, A. Conaty, A.M. da Silva, W. Gu, G. Kim, R. Koster, R. Lucchesi,
718 D. Merkova, J.E. Nielsen, G. Partyka, S. Pawson, W. Putman, M. Rienecker, S.D.
719 Schubert, M. Sienkiewicz, and B. Zhao, 2017: The Modern-Era Retrospective Analysis
720 for Research and Applications, Version 2 (MERRA-2). *J. Climate*, 30, 5419–5454,
721 <https://doi.org/10.1175/JCLI-D-16-0758.1>.

722 Griffies, S. M., Gnanadesikan, A., Dixon, K. W., Dunne, J. P., Gerdes, R., Harrison, M. J.,
723 Rosati, A., Russell, J. L., Samuels, B. L., Spelman, M. J., Winton, M., and Zhang, R.:
724 Formulation of an ocean model for global climate simulations, *Ocean Sci.*, 1, 45-79,
725 <https://doi.org/10.5194/os-1-45-2005>, 2005.

726 Huang, B., V.F. Banzon, E. Freeman, J. Lawrimore, W. Liu, T.C. Peterson, T.M. Smith, P.W.
727 Thorne, S.D. Woodruff, and H. Zhang, 2015: [Extended Reconstructed Sea Surface](#)
728 [Temperature Version 4 \(ERSST.v4\). Part I: Upgrades and Intercomparisons](#). *J. Climate*,
729 **28**, 911–930, <https://doi.org/10.1175/JCLI-D-14-00006.1>

730 Hunke, C. E. and W. Lipscomb, 2010: CICE: The Los Alamos sea ice model documentation and
731 software user's manual version 4.0 LA-CC-06-012. Tech. Rep. LA-CC-06-012

732 IPCC, 2013: *Climate Change 2013: The Physical Science Basis. Contribution of Working Group*
733 *I to the Fifth Assessment Report of the Intergovernmental Panel on Climate Change*
734 [Stocker, T.F., D. Qin, G.-K. Plattner, M. Tignor, S.K. Allen, J. Boschung, A. Nauels, Y.

735 Xia, V. Bex and P.M. Midgley (eds.)]. Cambridge University Press, Cambridge, United
736 Kingdom and New York, NY, USA, 1535 pp, doi:10.1017/CBO9781107415324.

737 Jong, B., M. Ting, R. Seager, N. Henderson, and D.E. Lee, 2018: Role of Equatorial Pacific SST
738 Forecast Error in the Late Winter California Precipitation Forecast for the 2015/16 El
739 Niño. *J. Climate*, 31, 839–852, <https://doi.org/10.1175/JCLI-D-17-0145.1>

740 Kirtman, Ben, Dughong Min, Johnna M. Infanti; James L. Kinter III; Daniel A. Paolino; Qin
741 Zhang; Huug van den Dool; Suranjana Saha; Malaquias Pena Mendez; Emily Becker;
742 Peitao Peng; Patrick Tripp; Jin Huang; David G. DeWitt; Michael K. Tippett; Anthony G.
743 Barnston; Shuhua Li; Anthony Rosati; Siegfried D. Schubert; Michele Rienecker; Max
744 Suarez; Zhao E. Li; Jelena Marshak; Young-Kwon Lim; Joseph Tribbia; Kathleen
745 Pegion; William J. Merryfield; Bertand Denis; Eric F. Wood, 2014: The North American
746 Multi-Model Ensemble (NMME): Phase-1 Seasonal to Interannual Prediction, Phase-2
747 Toward Developing Intra-Seasonal Prediction. *Bull. Am. Meteorol. Soc.* 95 585–601.

748 Koster, R. D., M. J. Suarez, A. Ducharne, M. Stieglitz, and P. Kumar, 2000: A catchment-based
749 approach to modeling land surface processes in a general model: 1. Model structure. *J.*
750 *Geophys. Res.*, 105(D20), 24809-24822, doi:10.1029/2000JD900327.

751 Lachmy, O. and N. Harnik, 2016: Wave and Jet Maintenance in Different Flow Regimes. *J.*
752 *Atmos. Sci.*, 73, 2465–2484, <https://doi.org/10.1175/JAS-D-15-0321.1>

753 Leith, C. E., 1978: Objective methods for weather prediction. *Annu. Rev. Fluid Mech.*, 10, 107–
754 128.

755 Lin, Y., W. Dong, M. Zhang, Y. Xie, W. Xue, J. Huang, Y. Luo, 2017: Causes of model dry and
756 warm bias over central U.S. and impact on climate projections. *Nature Communications*,

757 1-8, 10.1038/s41467-017-01040-2.

758 Molod, A. M., L. Takacs, M. Suarez, and J. Bacmeister, 2015: Development of the GEOS-5
759 atmospheric general circulation model: evolution from MERRA to MERRA2. *Geosci.*
760 *Model Dev.*, 8, 1339-1356, doi:10.5194/gmd-8-1339-2015.

761 Molod, A., E. Hackert, L. C. Andrews, R. M. Kovach, B. Zhao, Z. Li, Y.-K. Lim, A. Borovikov,
762 G. Vernieres, J. Marshak, R. Koster, J. Carton, R. Cullather, D. Barahona, S. Schubert, D.
763 Achuthavarier, Y. Vikhliav, J. L. M. Freire, K. M. Longo, 2018: GEOS-S2S Version 2:
764 The GMAO high resolution coupled model and assimilation system for seasonal
765 prediction. To be submitted to J. Geophysical Research.

766 Moorthi, S., and M. J. Suarez, 1992: Relaxed Arakawa-Schubert: A parameterization of moist
767 convection for general circulation models. *Mon. Wea. Rev.*, 120, 978-1002.

768 Orbe, C., L.D. Oman, S.E. Strahan, D.W. Waugh, S. Pawson, L.L. Takacs, and A.M. Molod,
769 2017: Large-scale atmospheric transport in GEOS replay simulations. *J. Adv. Model.*
770 *Earth Syst.*, 9, no. 7, 2545-2560, doi:10.1002/2017MS001053.

771 Putman, W., and S.-J. Lin, 2007: Finite-volume transport on various cubed-sphere grids. *J.*
772 *Comput. Phys.*, 227, 55–78, doi:https://doi.org/10.1016/j.jcp.2007.07.022.

773 Robinson, W. A., 1997: Dissipation dependence of the jet latitude. *J. Climate*, 10, 176–182.

774 Saha, S., 1992: Response of the NMC MRF model to systematic error correction within
775 integration. *Mon. Wea. Rev.*, 120, 345–360.

776 Schemm, J.-K., and A. Faller, 1986: Statistical corrections to numerical predictions. Part IV.
777 *Mon. Wea. Rev.*, 114, 2402–2417.

778 Schubert, S., H. Wang, and M. Suarez, 2011: Warm Season Subseasonal Variability and Climate
779 Extremes in the Northern Hemisphere: The Role of Stationary Rossby Waves, *J. Climate*,
780 24, 4773-4792.

781 Schubert, S., H. Wang, R. Koster, M. Suarez and P. Groisman 2014: Northern Eurasian Heat
782 Waves and Droughts. *Journal of Climate*. 27, 3169–3207.

783 Seager, Richard , Martin Hoerling, Siegfried Schubert, Hailan Wang, Bradfield Lyon, Arun
784 Kumar, Jennifer Nakamura, and Naomi Henderson, 2015: Causes of the 2011–14
785 California drought, *J. Climate*, 28, 6997–7024. doi: [http://dx.doi.org/10.1175/JCLI-D-](http://dx.doi.org/10.1175/JCLI-D-14-00860.1)
786 14-00860.1, 2015.

787 Seager, R. and N. Henderson, 2016: On the Role of Tropical Ocean Forcing of the Persistent
788 North American West Coast Ridge of Winter 2013/14. *J. Climate*, 29, 8027–8049,
789 <https://doi.org/10.1175/JCLI-D-16-0145.1>

790 Takacs, L.L., M.J. Suárez, and R. Todling, 2018: [The Stability of Incremental Analysis Update](https://doi.org/10.1175/MWR-D-18-0117.1).
791 *Mon. Wea. Rev.*, **146**, 3259–3275, <https://doi.org/10.1175/MWR-D-18-0117.1>

792 Wang, H. and S. Schubert, 2014: Causes of the Extreme Dry Conditions over California during
793 Early 2013, *Bull. Amer. Meteor. Soc.*, vol. 95, no. 9, Sept. 2014, p. S7-S11, 2014.

794 Wang, H., S.D. Schubert, and R.D. koster, 2017: North American Drought and Links to Northern
795 Eurasia: The Role of Stationary Rossby Waves. *Climate Extremes:Mechanisms and*
796 *Potential Prediction*, S. Wang et al. (Eds.), AGU Monograph, American Geophysical
797 Union.

798 Xue, H.-L., Shen, X.-S., & Chou, J.-F. (2013). A forecast error correction method in numerical
799 weather prediction by using the recent multiple-time evolution data. *Advances in*
800 *Atmospheric Sciences*, 30(5), 1249–1259. <https://doi.org/10.1007/s00376-013-2274-1>.

801 Yu H., J. Huang, W. Li, and G. Feng, 2014a: Development of the analogue-dynamical method
802 for error correction of numerical forecasts. *J. Meteor. Res.*, 28(5), 934-947, doi:
803 10.1007/s13351-014-4077-4.

804 Yu H., J. Huang, and J. Chou, 2014b: Improvement of medium-range forecasts using the
805 analogue-dynamical method. *Mon. Wea. Rev.*, 142(4), 1570-1587, doi:
806 <http://dx.doi.org/10.1175/MWR-D-13-00250.1>

807

808

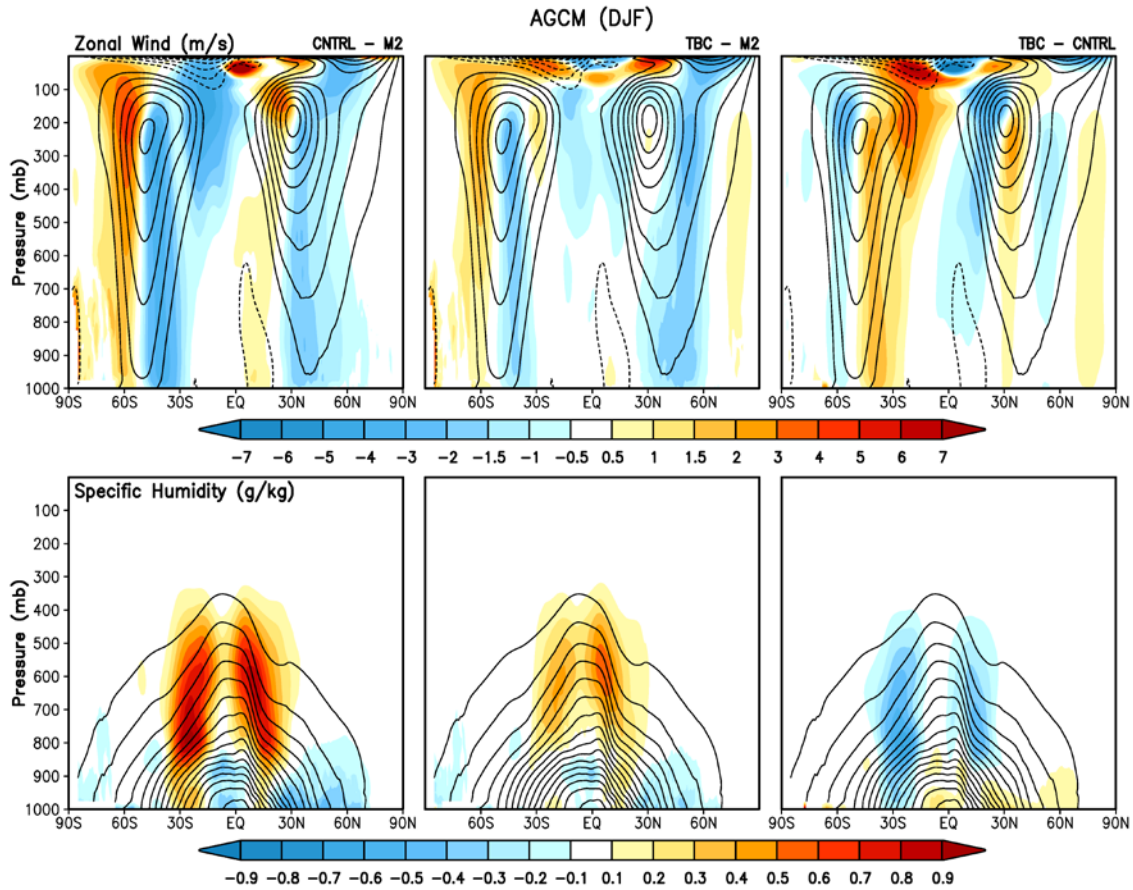
809 **Table 1.** A summary of the AGCM and AOGCM experiments.

Exp. #	Exp. Name	Description	Model	SST
1	CNTRL-A simulation	36- year control simulation for the period 1980-2015	AGCM without TBC	observed
2	TBC-A simulation	36- year TBC simulation for the period 1980-2015	AGCM with TBC	observed
3	CNTRL-A hindcasts	hindcasts initiated every day from May 1-June 30 and run through the end of August for 1988, 1998 and 2000-2015	AGCM without TBC	observed
4	TBC-A hindcasts	hindcasts initiated every day from May 1-June 30 and run through the end of August for 1988, 1998 and 2000-2015	AGCM with TBC	observed
5	CNTRL-C simulation	36- year control simulation for the period 1981-2016	AOGCM without TBC	predicted
6	REPLAY-C simulation	36- year replay to MERRA-2 for the period 1981-2016	AOGCM replayed to MERRA-2	predicted
7	TBC-C simulation	36- year simulation with TBC for the period 1981-2016	AOGCM with TBC	predicted
8	CNTRL-C hindcasts	10-member ensemble hindcasts initialized every November 1 and run through April 1 of the following year for 1985-2015	AOGCM without TBC	predicted
9	TBC-C hindcasts	10-member ensemble hindcasts initialized every November 1 and run through April 1 of the following year for 1985-2015	AOGCM with TBC	predicted

810

811

812



813

814 Figure 1: The zonal mean u-wind (top panels, m/s) and specific humidity (bottom panels, g/kg).

815 Left panels: the shading indicates CNTRL-A – MERRA-2 with the climatological MERRA-2

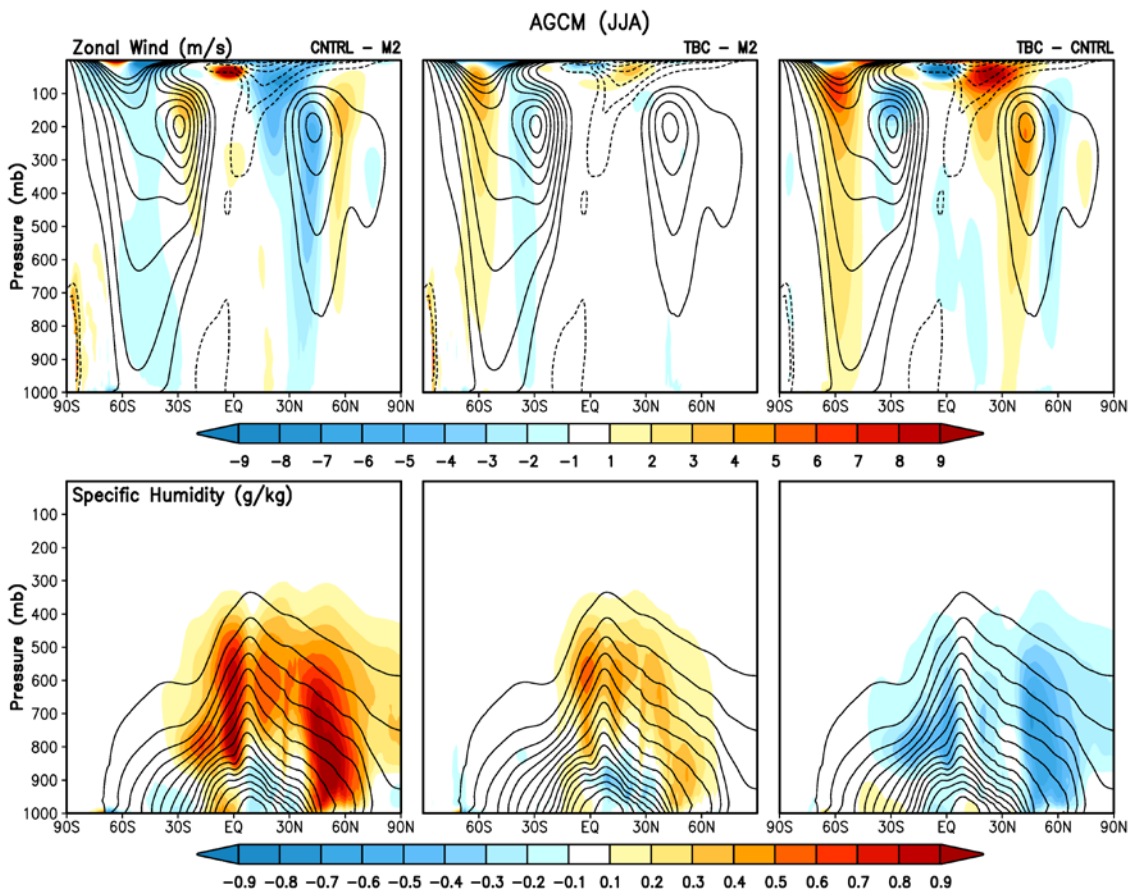
816 wind fields contoured every 5 m/s in the top panels, and the MERRA-2 climatological specific

817 humidity contoured every 1 g/kg in the bottom panels. Middle panels are the same as the left

818 panels, except for TBC-A - MERRA-2. Right panels are the same as the left two panels, except

819 for TBC-A – CNTRL-A. All fields are averaged for DJF over the years 1980-2015.

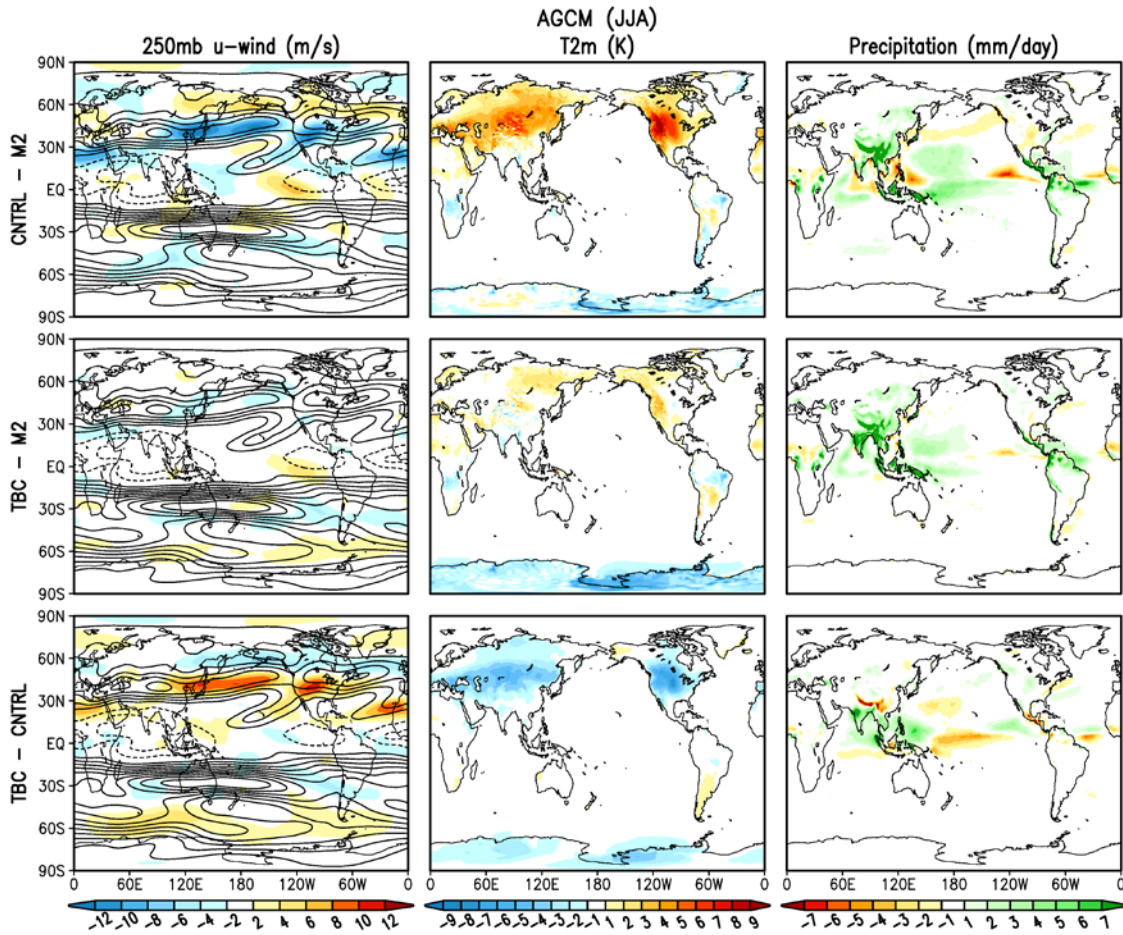
820



821

822 Figure 2: Same as Fig. 1, except for JJA.

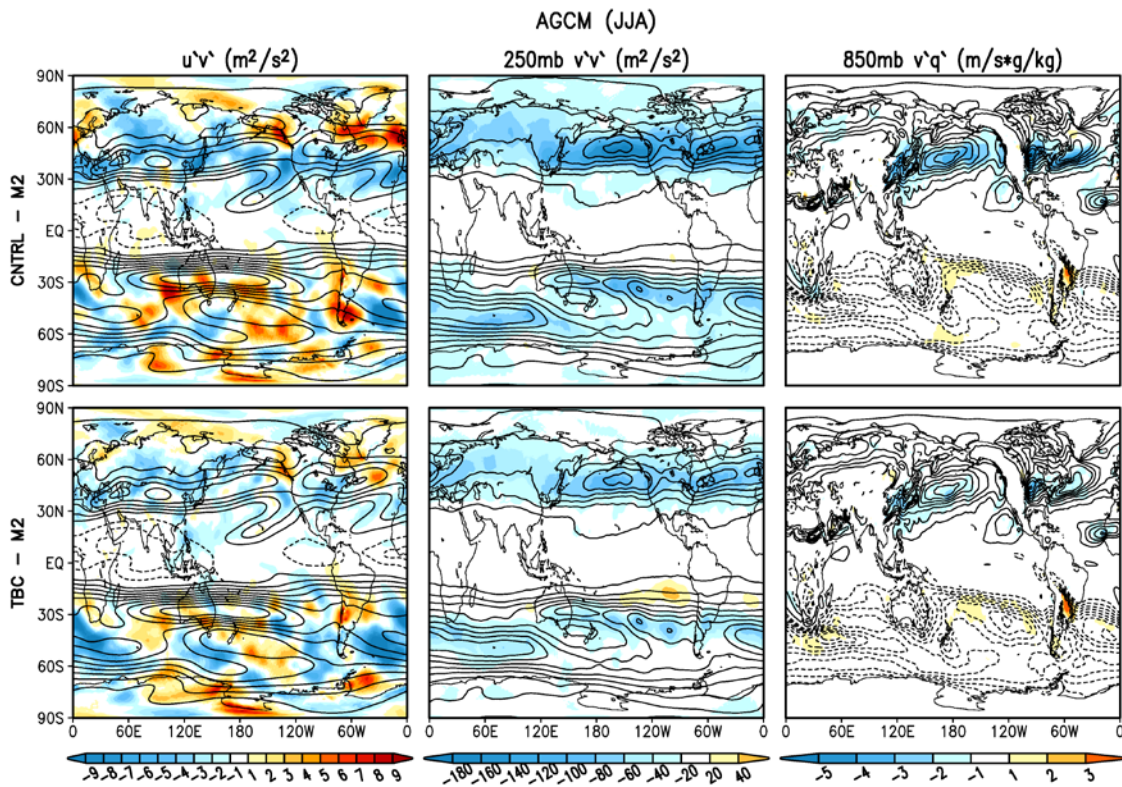
823



824

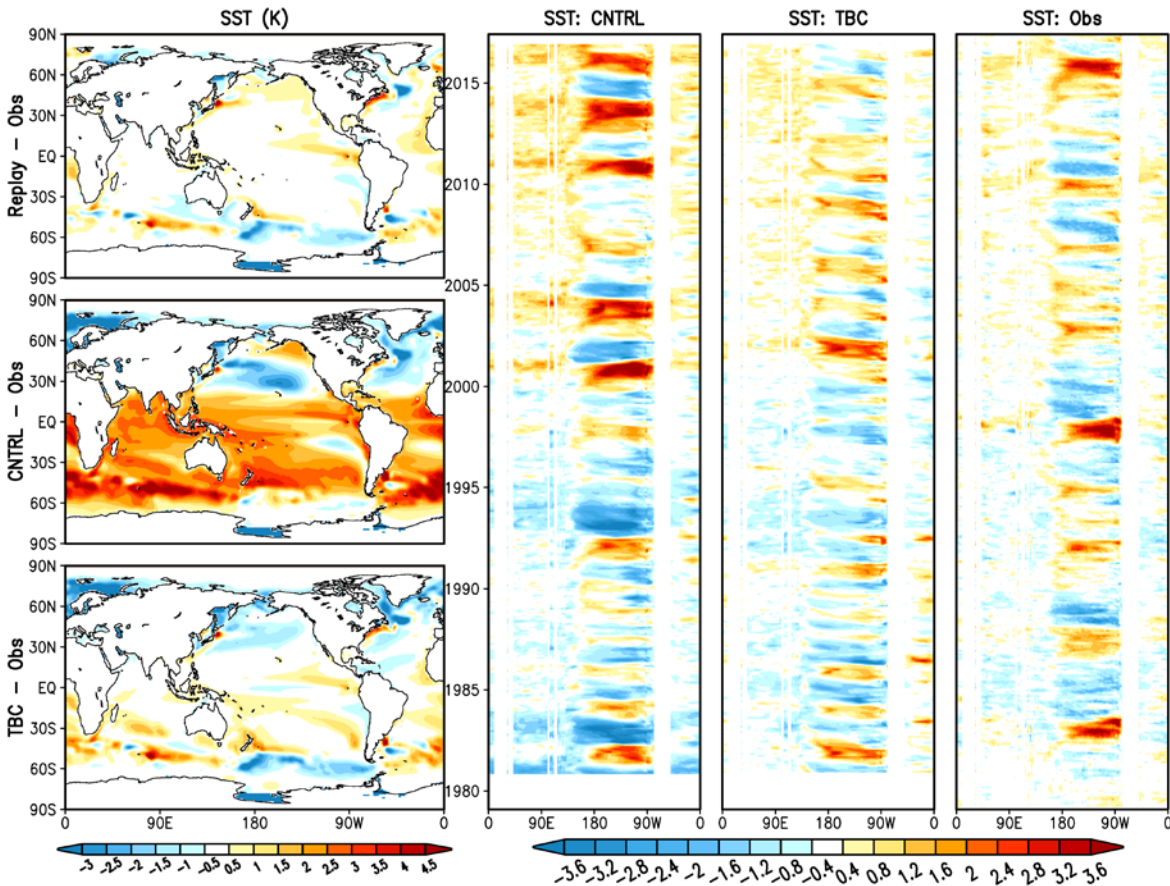
825 Figure 3: The 250mb zonal wind (m/s, left column of panels), two-meter temperature ($^{\circ}$ K,
 826 middle column of panels), and precipitation (mm/day, right column of panels). The shading
 827 indicates the CNTRL-A – MERRA-2 in the top row of panels, TBC-A - MERRA-2 in the middle
 828 row of panels, and TBC-A – CNTRL-A in the bottom row of panels. In the left panels the
 829 contours indicate climatological mean 250mb zonal winds from MERRA-2 (contoured every 5
 830 m/s). All fields are averaged for JJA over the years 1980-2015. The MERRA-2 precipitation is
 831 an observationally-corrected field (Gelaro et al. 2017).

832



833

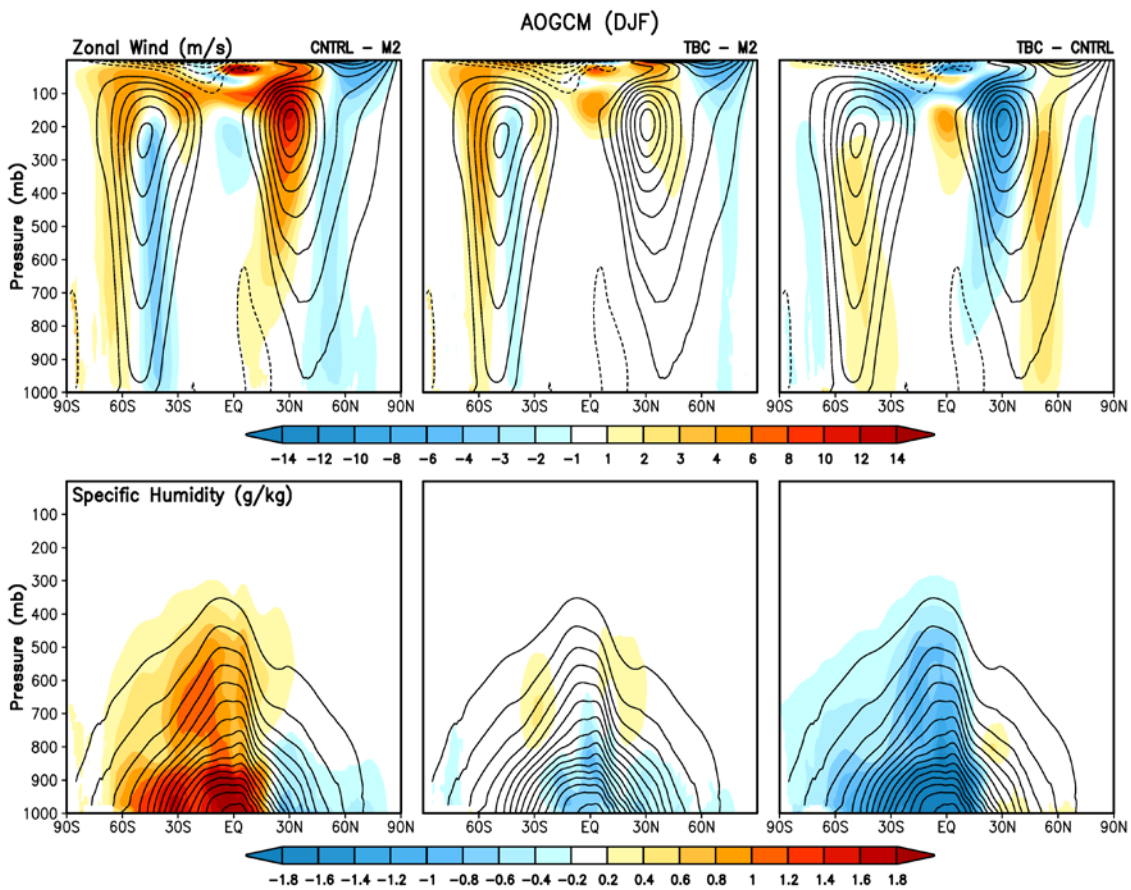
834 Figure 4: The vertically-integrated momentum flux by the transients ($(\text{m/s})^2$, left panels), the
 835 250mb square of the transient component of the meridional wind ($(\text{m/s})^2$, middle panels), and the
 836 850mb moisture flux by the transients (g/kg m/s , right panels). The shading indicates CNTRL-A
 837 – MERRA-2 in the top panels, and TBC-A – MERRA-2 in the bottom panels. In the left panels
 838 the contours are the 250mb climatological zonal wind from MERRA-2 (every 5 m/s). In the
 839 middle panels the contours indicate the long-term mean of the 250mb square of the transient
 840 component of the meridional wind from MERRA-2 (every $50 (\text{m/s})^2$). In the right panel the
 841 contours indicate the long-term mean of the 850mb moisture flux by the transients from
 842 MERRA-2 (every 1 g/kg m/s).



843

844 Figure 5: Left panels: the long term mean SST bias with respect to observations (ERSST.v4:
 845 Huang et al. 2015). Results are shown for REPLAY-C (top panel), CNTRL-C (middle panels),
 846 and TBC-C (bottom panel). Right panels: evolution of the monthly mean equatorial SST
 847 anomalies (2°S-2°N) from 1980-2016, for CNTRL-C, TBC-C, and the observations. Units: °K.
 848 Units: °K. All fields are averaged over the years 1981-2016.

849



850

851 Figure 6: The zonal mean u-wind (top panels, m/s) and specific humidity (bottom panels, g/kg).

852 Left panels: the shading indicates CNTRL-C – MERRA-2 with the climatological MERRA-2

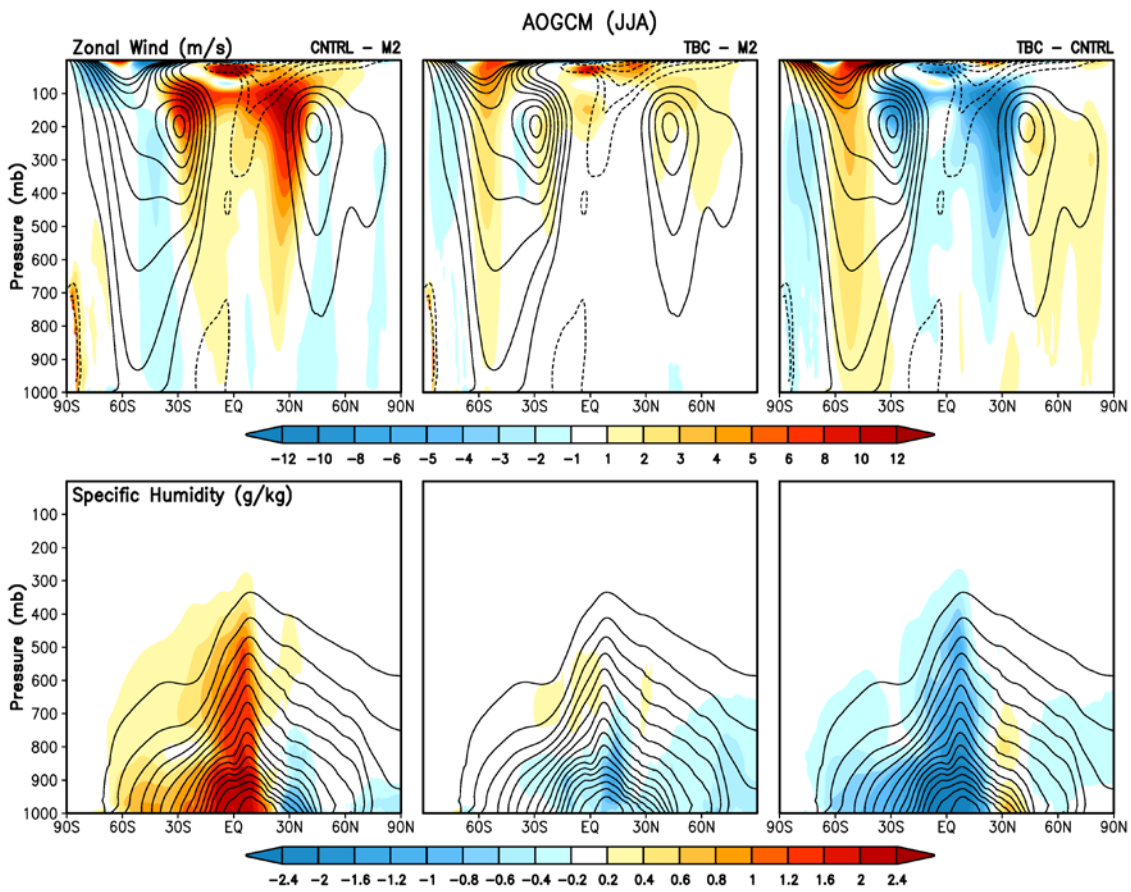
853 wind fields contoured every 5 m/s in the top panels, and the MERRA-2 climatological specific

854 humidity contoured every 1 g/kg in the bottom panels. Middle panels are the same as the left two

855 panels, except for TBC-C - MERRA-2. Right panels the same as the left two panels, except for

856 TBC-C – CNTRL-C. All fields are averaged for DJF over the years 1980-2015.

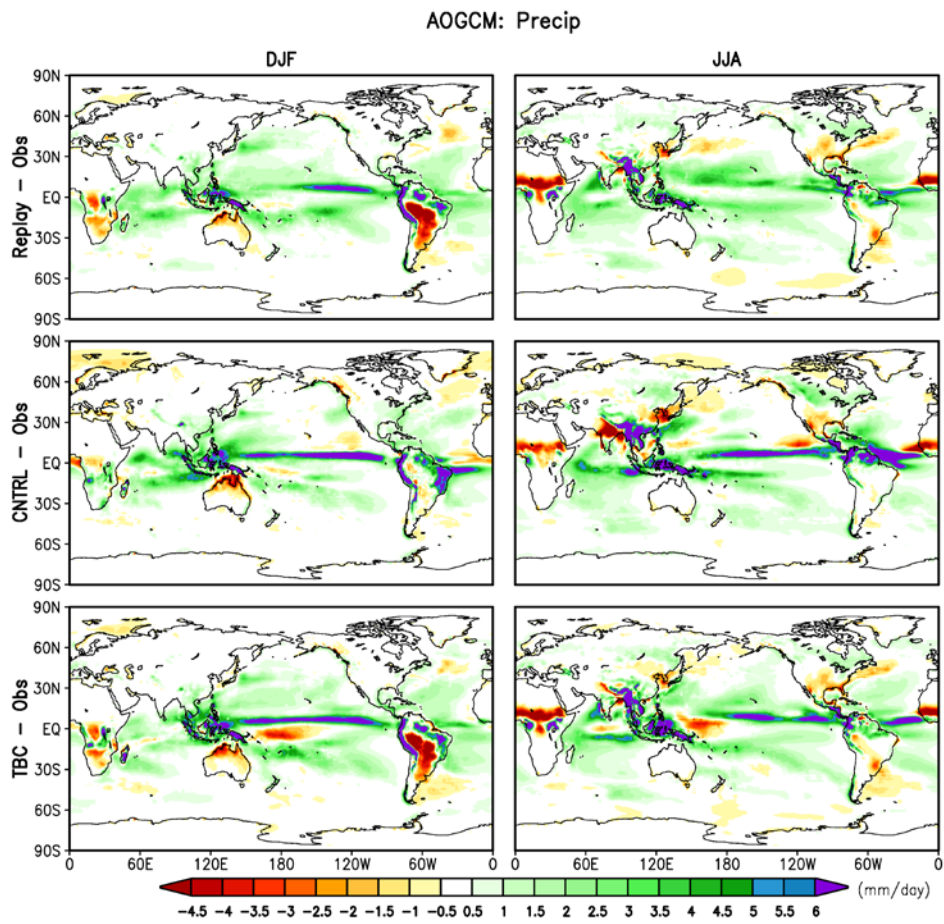
857



858

859 Figure 7: Same as Fig. 6, except for JJA.

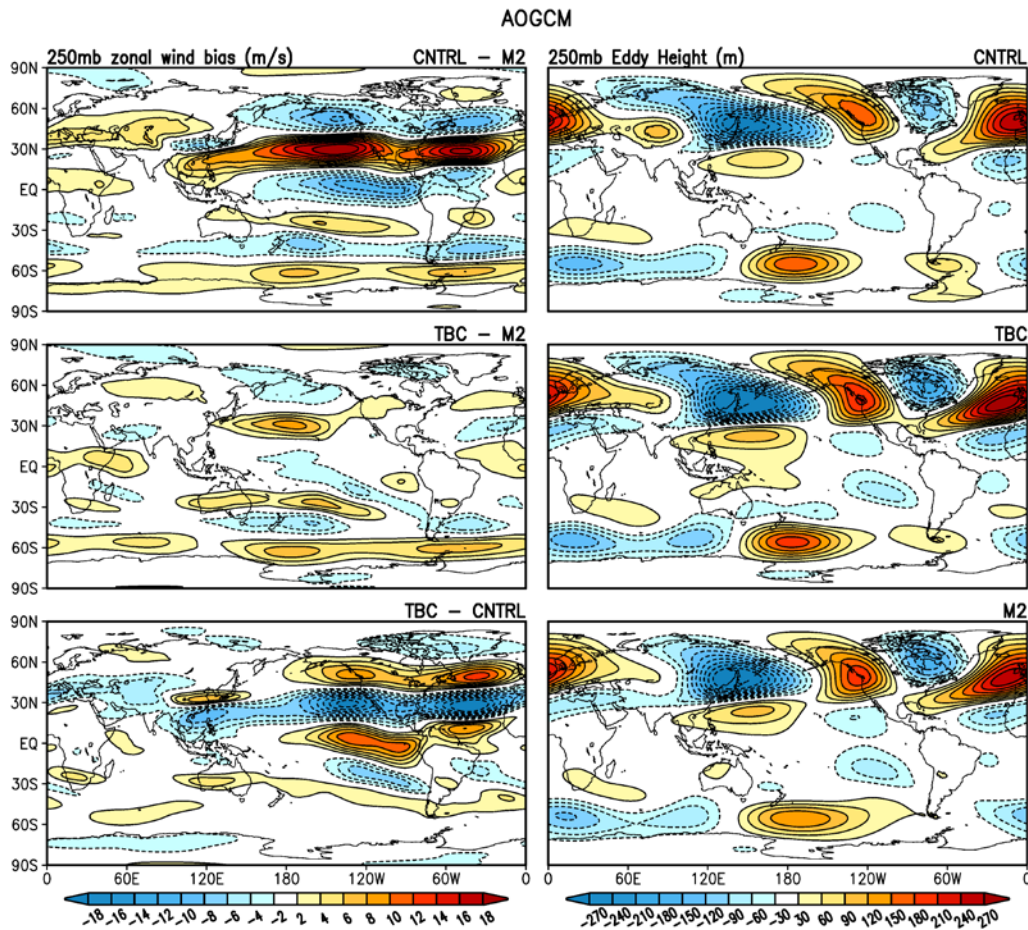
860



861

862 Figure 8: The precipitation biases (mm/day) with respect to MERRA-2 observationally
 863 corrected precipitation for DJF (left panels) and JJA (right panels). Results are shown for the
 864 replay run (top panel), the control (middle panels), and the TBC run (bottom panel). All fields
 865 are averaged over the years 1981-2016.

866



867

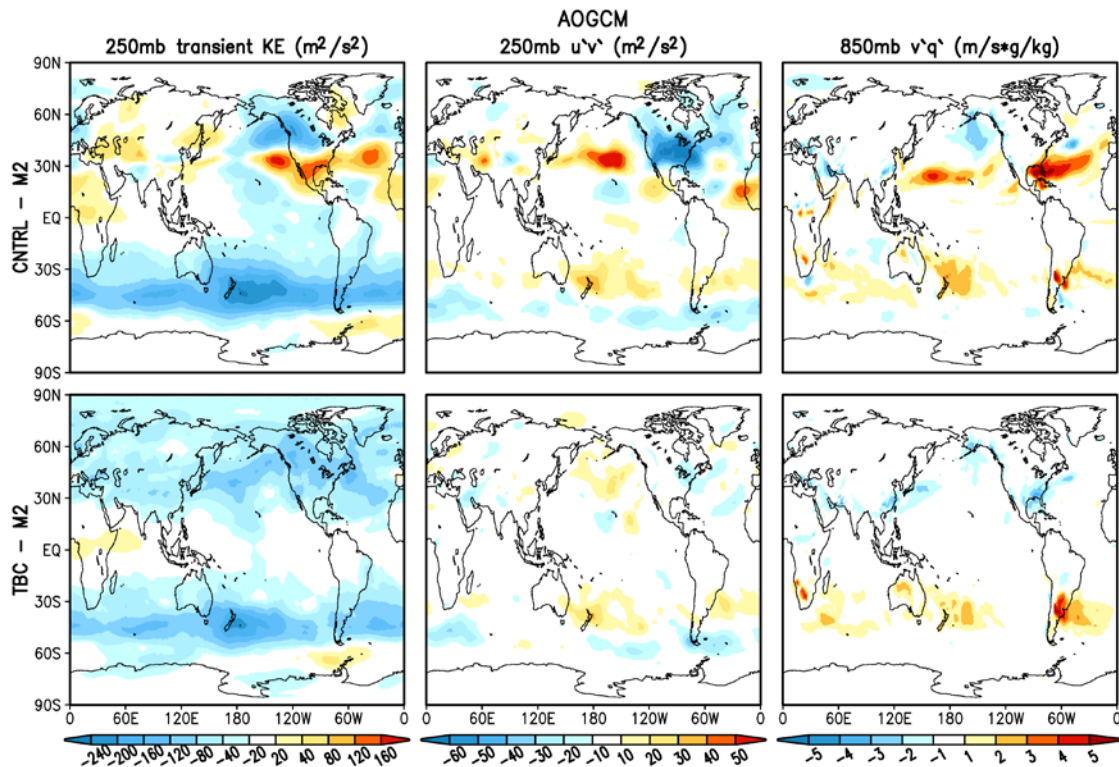
868 Figure 9: Left panels: the DJF zonal wind biases with respect to MERRA-2 for CNTRL-C (top)

869 and TBC-C (middle). The bottom panels show TBC-C – CNTRL-C. Units are m/s. Right

870 panels: the DJF stationary waves (250mb height with the zonal mean removed) for CNTRL-C

871 (top), TBC-C (middle), and MERRA-2 (bottom). Units are meters.

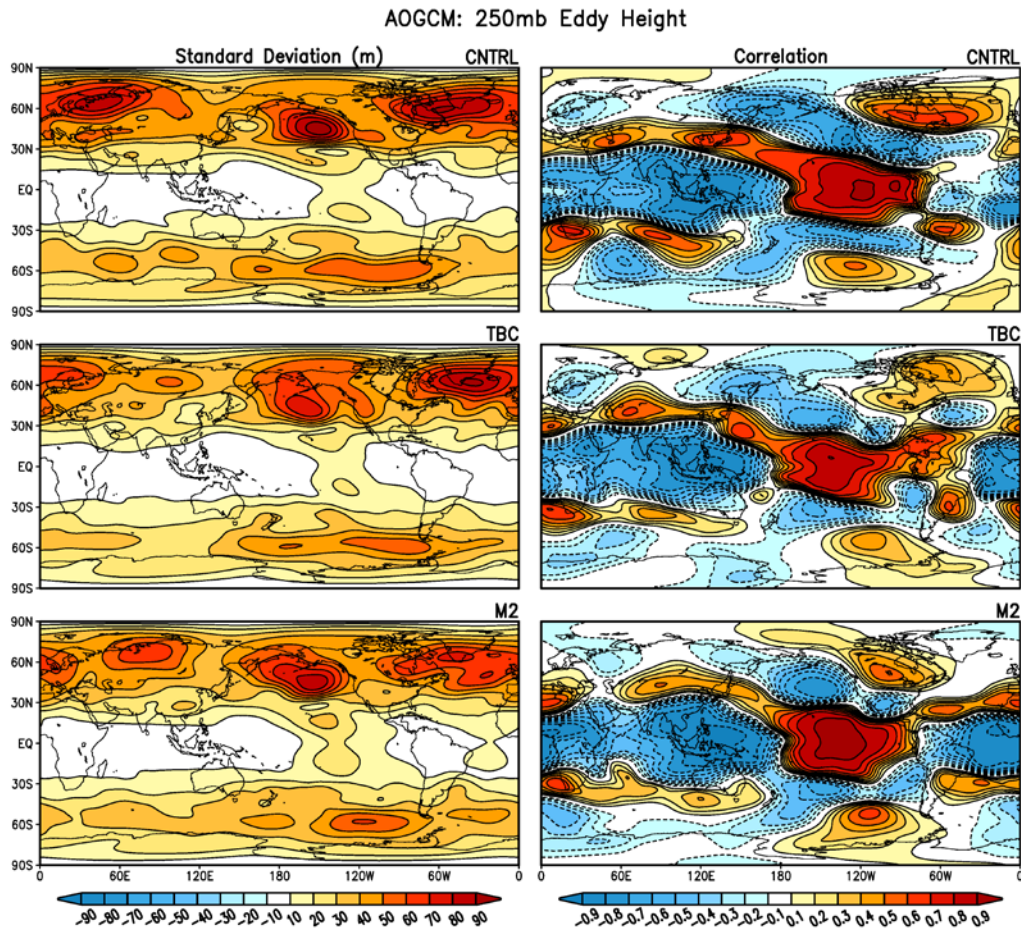
872



873

874 Figure 10: Left panels: CNTRL-C – MERRA-2 (top) and TBC-C – MERRA-2 (bottom) of the
 875 250mb kinetic energy associated with the transient component of the winds (m/s)². Middle
 876 panels: same as left panels, but for the 250mb zonal momentum flux by the transients (m/s)².
 877 Right panels: same as left panels but for the 850mb moisture flux by the transients (g/kg m/s).
 878 All fields are averaged for DJF over the years 1981-2016.

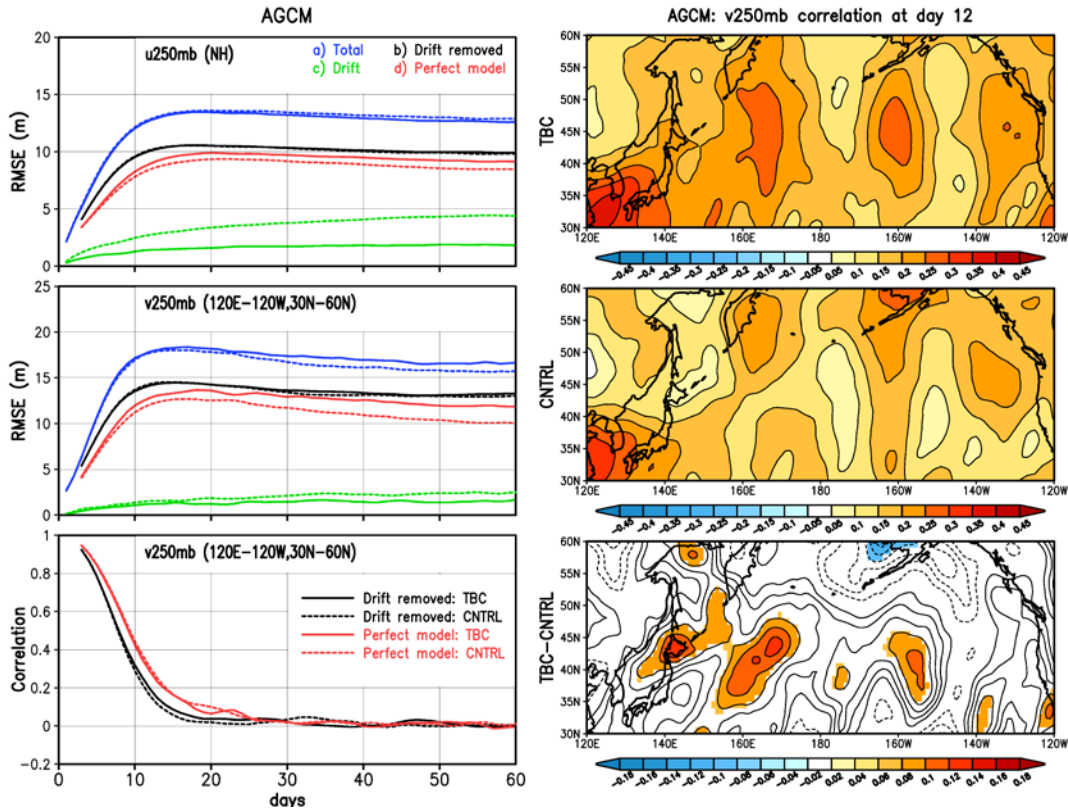
879



880

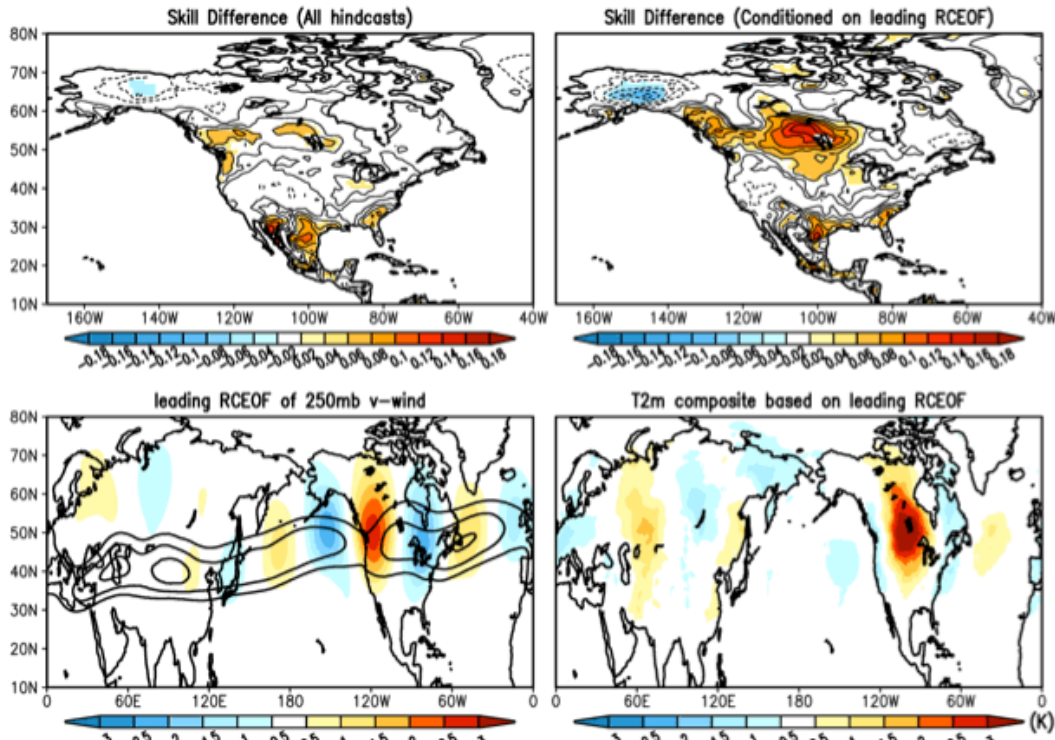
881 Figure 11: Left panels: the standard deviation (1981-2016) of the DJF mean stationary waves
 882 (250mb height with the zonal mean removed) for CNTRL-C (top), TBC-C (middle), and
 883 MERRA-2 (bottom). Units: m. Right panels: the correlations between the DJF mean Nino3.4
 884 index and the 250mb eddy height field for the CNTRL-C (top), TBC-C (middle) and MERRA-2
 885 (bottom).

886

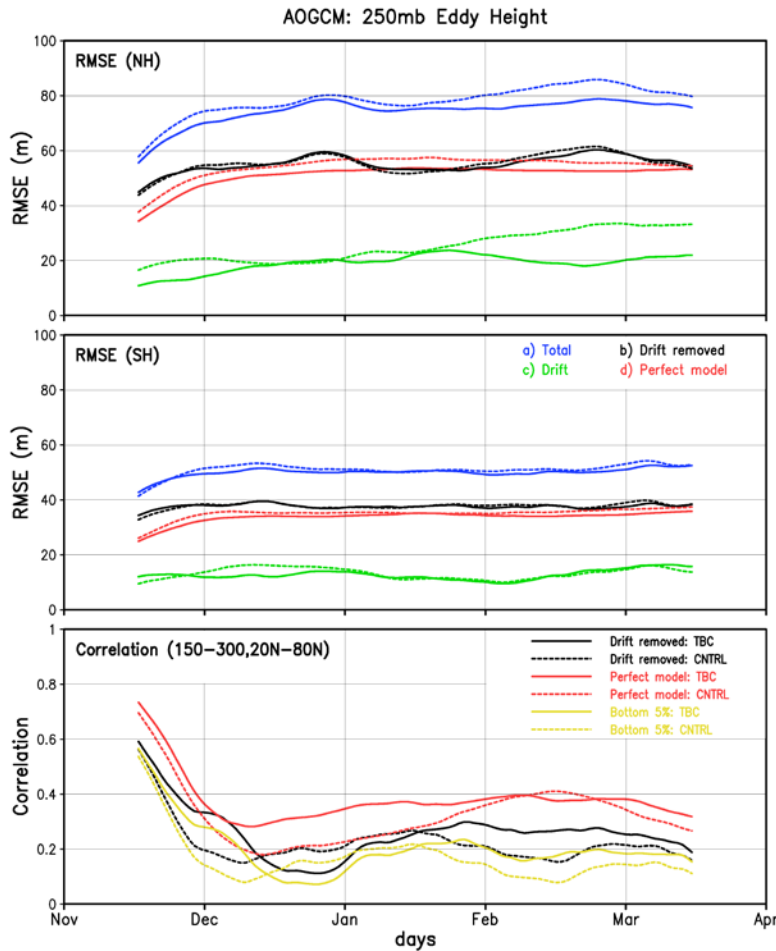


887

888 Figure 12: left panels: The RMSE decomposed according to (1) in the text for the daily 250mb u-
 889 wind for the NH (upper panel), and for the daily 250mb v-wind over the region (120E-120W,
 890 30N-60N) in the middle panel. In the bottom panel, the black curves show the v250mb
 891 correlations with MERRA-2 (while the red curves are the correlations for a perfect model), for
 892 the same region (120E-120W, 30N-60N). The dashed lines are for the control hindcasts, and the
 893 solid lines are for the TBC hindcasts. Units for RMSE are m/s. Abscissa indicates days. Right
 894 panels: The v250mb correlations at 12 day lead for TBC-A, CNTRL-A and the differences.
 895 Shading of the differences indicates a significance level of 0.10 based on a Fisher's z-transform.
 896 Results are based on predictions initialized every day from May 1 to June 30 in 1988, 1998,
 897 2000-2015. Five-member ensemble means are computed from lags -2,-1,0, 1, 2 days. See text
 898 for details.

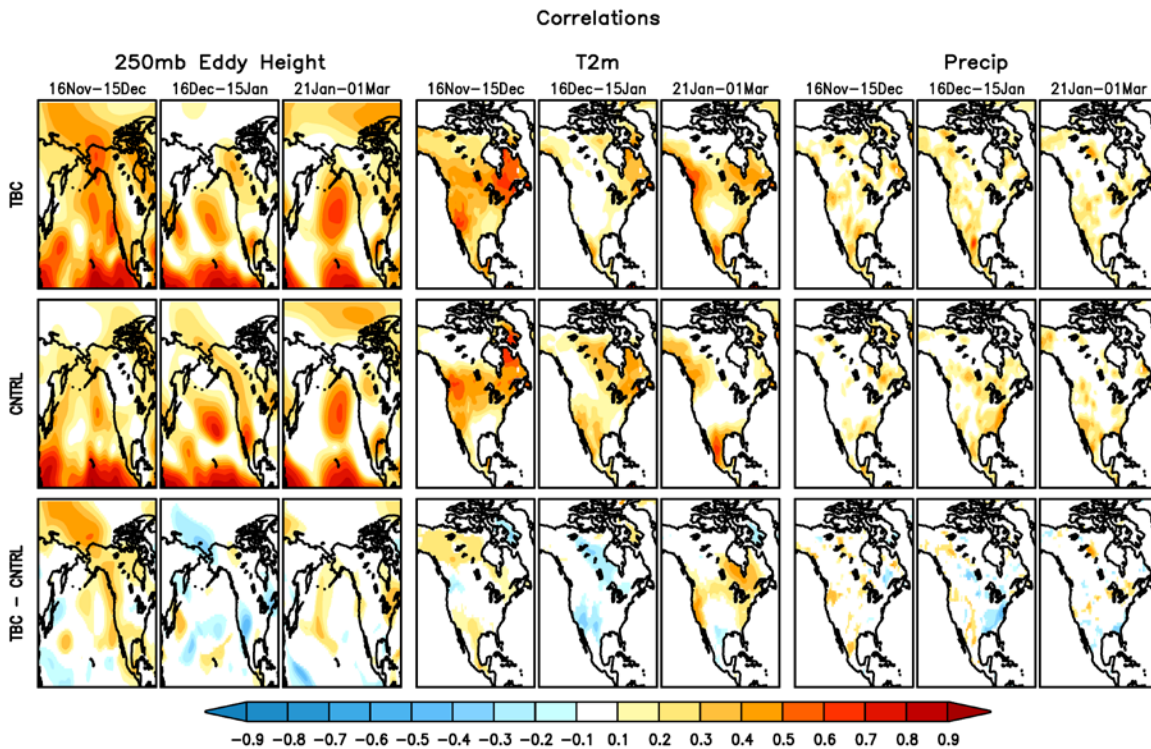


899 Figure 13: Top left panel: Differences in skill (correlation between the hindcasts and MERRA-2)
 900 at day 10 day between TBC-A and CNTRL-A based on all the hindcasts. Shading indicates a
 901 significance level of 0.10 based on a Fisher's z-transform. Top right panel: same as top left,
 902 except for only those hindcasts when the leading Rossby wave has an amplitude greater than 1
 903 standard deviation in the initial conditions. Bottom left panel: The leading rotated complex
 904 empirical orthogonal function (RCEOF) of the NH (10N-80N) daily (filtered with a 11-day
 905 running mean) 250mb meridional wind anomalies during MJJA computed from MERRA-2 for
 906 the period 1980-2017 (see Chang et al. 2001 for details of the RCEOF calculation). The
 907 contours (15, 20 and 25 m/s) are the long-term mean MJJA 250mb zonal wind based on
 908 MERRA-2. The phase of the RCEOF plotted here is chosen to highlight that phase during which
 909 the wave has the greatest impact on North America (bottom right). The values of the RCEOF
 910 (m/s) and T2m (°C) correspond to composites based on those times when the associated rotated
 911 complex principle component (RCPC) exceeded 1 standard deviation.
 912



913

914 Figure 14: The RMSE decomposed according to (1) in the text for the 250mb eddy height for
 915 the NH (top) and SH (middle). The dashed lines are for the CNTRI-C hindcasts, and the solid
 916 lines are for the TBC-C hindcasts. Units are meters. Bottom panels show the PNA region
 917 250mb eddy height correlations with MERRA-2 (black lines) and for a perfect model (red lines).
 918 The yellow lines, which are the bottom 5% of the correlations with MERRA-2 obtained from all
 919 combinations of removing 5 years from the 31 years of data (total of 169911), give an indication
 920 of the robustness of the 250mb eddy height correlations with MERRA-2. The daily fields have a
 921 31-day running mean applied to remove weather and other sub-monthly noise. Results are based
 922 on 10 ensemble members initialized November 1 of 1985-2015.

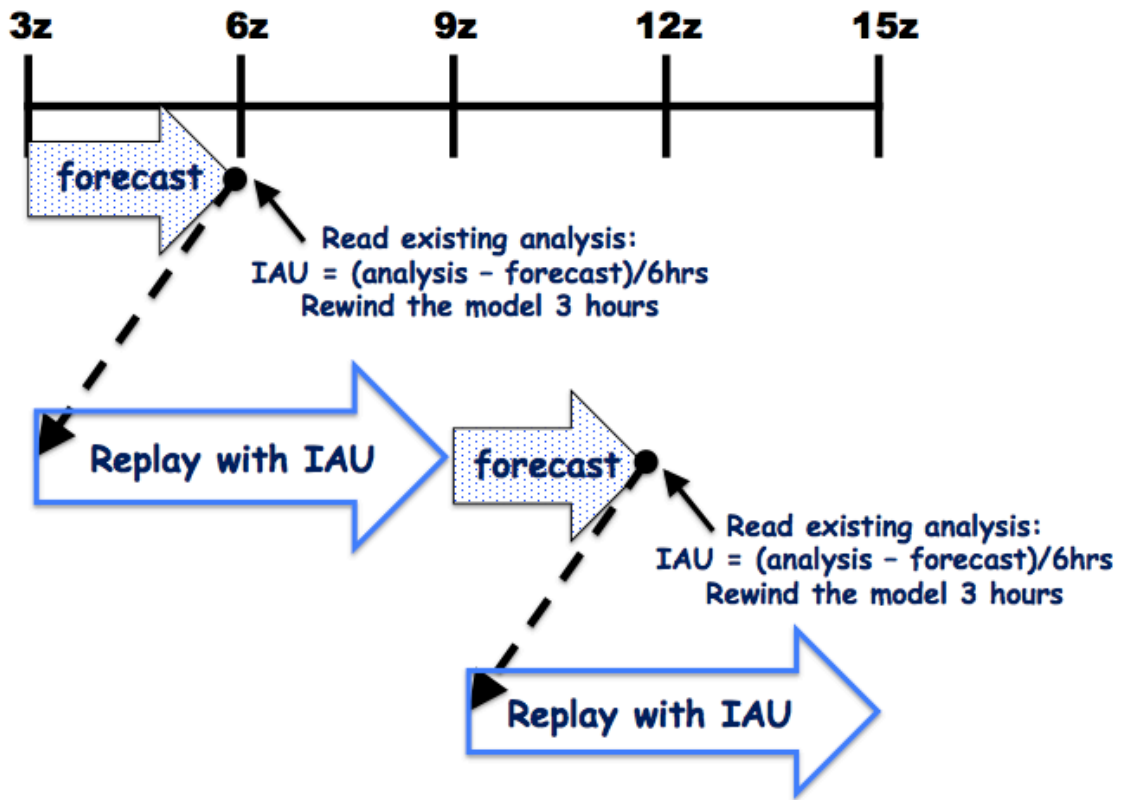


923

924 Figure 15: Maps of the correlations (only where values are greater than 0) between the hindcast
 925 ensemble mean and observations for 250mb eddy height (left 9 panels), T2m over North
 926 America (middle 9 panels), and precipitation over North America (right 9 panels). Results are
 927 based on 10 ensemble members initialized November 1 of the years 1985-2015. Top panels are
 928 for the TBC-C hindcasts, and middle panels are for the CNTRL-C hindcasts. The bottom panels
 929 are the differences in the correlations between the TBC-C and CNTRL-C hindcasts. Shading
 930 indicates a significance level of 0.10 based on a Fisher's z-transform. Results are shown for
 931 averages over the following time periods: 16Nov-15Dec, 16Dec-15Jan, and 21Jan - 01Mar.

932

GMAO Replay Cycle with IAU



933

934 Figure A1: Schematic of the replay procedure used by the GMAO.